# Proton-Carbon Polarimetry at RHIC

I. Nakagawa [a,b,*] O. Jinnouchi [b,4] A. Bravar [d,1] I. Alekseev [c] A. Bazilevsky [d] G. Bunce [d,b] C. Muñoz Camacho [e] S. Dhawan [h] K.O. Eyser [i] R. Gill [d] H. Huang [d] H. Liu [e] M.X. Liu [e] K. Kurita [g] Y. Makdisi [d] A. Nass [d,2] H. Okada [f,3] W. Haeberli [j] T. Wise [j] N. Saito [f,4] D.N. Svirida [c] J. Wood [d] K. Yip [d] A. Zelenski [d]

[a] *Nishina Center for Accelerator-Based Science, RIKEN, Wako, Saitama, 351-0198, Japan*
[b] *Riken BNL Research Center, Upton, NY 11973, USA*
[c] *Institute for Theoretical and Experimental Physics, Moscow, Russia*
[d] *Brookhaven National Laboratory, Upton, NY 11973, USA*
[e] *Los Alamos National Laboratory, Los Alamos, NM 87545, USA*
[f] *Kyoto University, Kyoto 606-8502, Japan*
[g] *Rikkyo University, Tokyo, 171-8501, Japan*
[h] *Yale University, New Haven, CT 06520, USA*
[i] *University of California, Riverside, CA 92521, USA*
[j] *University of Wisconsin, WI 53706, USA*

**Abstract**

Polarimeters were developed to measure the polarization of the proton beam at the Relativistic Heavy Ion Collider (RHIC) in relative scale through the asymmetry measurement of elastic proton-carbon scattering. The Coulomb-nuclear interfarance (CNI) region was chosen for the polarimetry, where a significant asymmetry was predicted due to the one photon exchange amplitude that generates the proton's anomalous magnetic moment. Recoil carbon ions with kinetic energy of $400 \leq E \leq 900$ keV were detected by silicon strip detectors installed near 90° with respect to the beam. The absolute polarization is given by normalizing against another polarimeter implemented at RHIC, namely a polarized hydrogen gas jet polarimeter. In this report, the details of polarization measurements, data analysis, and systematic uncertainties are discussed based on the data taken during $\sqrt{s} = 200$ GeV operation of 2006 running (Run06) at RHIC.

*Key words:* polarized proton, silicon strip detector, RHIC, polarimeter, polarimetry, CNI, forward elastic scattering
*PACS:* 13.88.+e, 29.27.Hj

## 1. INTRODUCTION

The polarization of the proton beams(1; 2) at the Relativistic Heavy Ion Collider (RHIC)(3) is measured using both a polarized atomic beam source hydrogen gas jet (H-Jet)(5; 6; 8) and proton-carbon (pC) polarimeters(9; 10). RHIC consists of two counter rotating accelerator/storage rings with six crossings labeled as 2,4,6,8,10, and 12 o'clock where collisions may take place. Each rings are built on a common horizontal plane, one ("Blue Ring") for clockwise and the other ("Yellow Ring") for counter-clockwise beams.

The polarimeters are set up in the 12 o'clock collision area (IP12). The H-Jet polarimeter is located at the collision point allowing measurements of both beams. Two identical pC polarimeters are installed in separate RHIC storage rings. The pC-polarimeter detects recoil carbon ions through the proton-carbon elastic scattering reaction and measures relative polarization of polarized proton beam from the left-right asymmetry of observed carbon yields. Each measurement is done to a few percent statistical accuracy within 20 to 30 seconds using an ultra-thin (typically $6 \sim 8$ $\mu$g/cm$^2$) carbon ribbon target, providing fast feedback to beam operations and experiments. Sufficient statistics also allows us to observe microscopic structures of the beam such as the polarizations of individual beam RF bunches and the transverse polarization profiles across the beam. The H-Jet polarimeter detects recoil protons through elastic proton-proton scattering, observing left-right asymmetries originated from the beam as well as target polarizations, simultaneously. The target polarization is continuously monitored by a built in Briet-Rabi polarimeter independently within the precision of 2%, providing the calibration of absolute scale of the analyzing power $A_{\rm N}^{\vec{\rm p}{\rm p}}$ for the elastic proton-proton scattering. Thus the H-Jet polarimeter measures the beam polarization in absolute scale using the self calibrated $A_{\rm N}^{\vec{\rm p}{\rm p}}$, yet with less statistical abundance compared to pC polarimeters, i.e. $\Delta P_{\rm H-Jet}/P_{\rm H-Jet}$ $\sim$5% in 1 to 2 days (as of Run06).

Such a self calibrated manner wouldn't be applied for pC polarimeters, they are normalized against the H-Jet polarimeter by running the pC and the H-Jet polarimeters for the same period. While H-Jet is the continuous measurement, pC polarimeter is the instantaneous and destructive measurement. Relevant weight on the beam intensity and duration of consecutive pC measurements were taken into account to calculate the average polarization from multiple pC measurements. The normalization factor is calculated by taking the ratio of average polarizations between the pC and H-Jet polarimeters. Once the pC polarimeter is normalized, then it functions as the absolute polarimeter and it provides absolute beam polarizations solo regardless the H-Jet was operated or not, simultaneously.

The published data of the analyzing power for the elastic polarized proton-carbon scattering is available up to the proton beam energy of 21.7 GeV/$c$(11). There are no published data available at the storage (flat-top) proton beam energy of 100 GeV where the colliding experiment was performed in RHIC. Shown in Fig. 1 is the analyzing power

* Tel.:+1 631 344 5984; fax: +1 631 344 2562
*Email address:* itaru@riken.jp (I. Nakagawa).
[1] Present Address: University of Geneva, 1205 Geneva, Switzerland
[2] Present Address: University of Erlangen, 91058 Erlangen, Germany
[3] Present Address: Brookhaven National Laboratory, Upton, NY 11973, USA
[4] Present Address: KEK, Tsukuba, Ibaraki 305-0801, Japan

at the beam energy of 100 GeV measured by the blue carbon polarimeter during a Run04 operation for the extended range of the momentum transfers $-t$. The absolute scale is given by the normalization against the average polarization of Run04 measured by the H-Jet polarimeter. Although $-t$ dependence of $A_{\rm N}$ is well determined by the data with sufficient statistics accumulated by the pC polarimeter, the precision of the absolute scale was limited by the statistical accuracy of the H-Jet measurement $\Delta A_{\rm N}^{\rm Run04}/A_{\rm N}^{\rm Run04} \sim \pm 9$ %. The strategy is to improve the accuracy year by year with more statistical abundance in the average polarization measurements by the carbon [5] $\overline{P_{\rm pC}^{\rm Run06}}$ and the hydrogen $\overline{P_{\rm H-Jet}^{\rm Run06}}$ polarimeters. The improved analyzing power of Run06 $A_{\rm N}^{\rm Run06}$ is given by

$$A_{\rm N}^{\rm Run06} = A_{\rm N}^{\rm Run04} \frac{\overline{P_{\rm pC}^{\rm Run06}}}{\overline{P_{\rm H-Jet}^{\rm Run06}}}. \quad (1)$$

The curves in the Fig. 1 are the model predictions(12) of with (blue) and without (red) the spin-flip amplitude fitted to the data. The analyzing power for the elastic polarized proton-carbon scattering is predicted to be maximized at the momentum transfer of ($-t \sim 0.003$ (GeV/c)$^2$) due to the interference between the electromagnetic and the strong (CNI) amplitudes. While electromagnetic part of the amplitude is exactly calculable by QED, the spin flip strong amplitude, which is demonstrated to play crucial role to fit data, is not well understood at this high energy. Measuring the polarization in the CNI region thus provides great advantage in terms of maximum sensitivity. To be as small $|t|$ as possible, the recoil carbon atoms were thus detected near 90 degrees with respect to the beam direction. Kinetic energy range is selected from 400 to 900 keV, whose corresponding momentum transfer is $0.009 \leq -t \leq 0.023$ (GeV/c)$^2$. The lower the kinetic energy, the larger the analyzing power and the more sensitivity we gain. The optimization of the energy range is the consequence of the trade off between the amplitude of the analyzing power and the reliability of the energy measurement of the low energy carbon ions. Details are discussed in section 3.2. Since there is a $t$-dependence in the analyzing power, the relative energy of recoil carbon ion needs to be measured to define the kinematics. An alternative option to detect the forward scattered proton instead of the low energy recoil carbon ion is even more difficult choice because of the tiny transverse kick given by $-t$ in CNI region. The scattered proton goes too close to the primary beam and is unrealistic within the present divergence of the beam.

In this paper, the experimental apparatus and online polarizations are described in Section 2. The calibration of detectors and energy correction are discussed in Section 3. Event selection and background contribution are discussed in Section 4. The calculation of polarizations from observed asymmetries is discussed in Section 5. In Section 6, the intrinsic difference of observed polarizations between pC and H-Jet polarimeters are explained and the necessity of the polarization profile correction for the normalization is raised. Further polarization profile correction is introduced to apply the measured polarizations by pC polarimeters to experiments. This is discussed in Section 7. Uncertainties are evaluated and summarized in Section 7. Section 8 is the summary the paper.

[5] Run04 $A_{\rm N}$ was still employed to evaluate online polarizations during Run06.

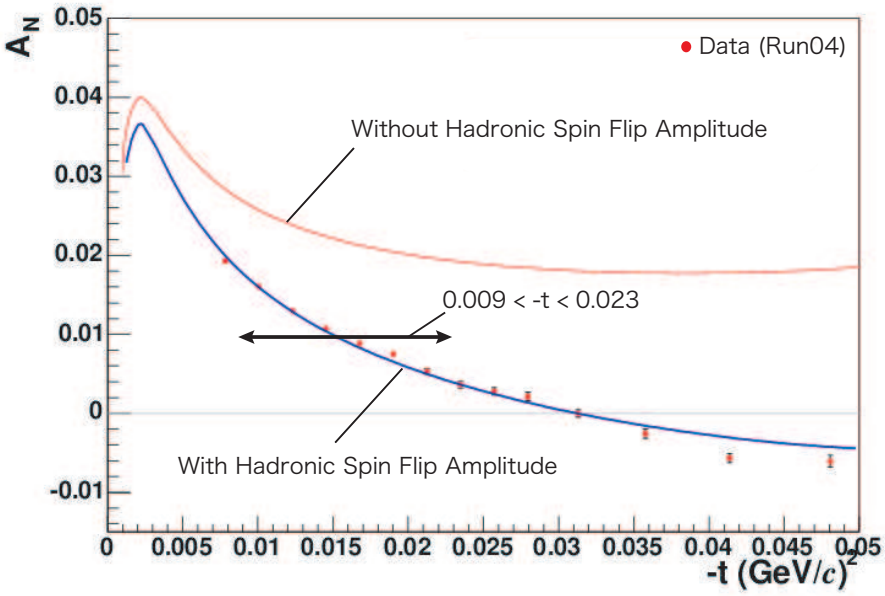


Fig. 1. The analyzing power measured by the blue pC polarimeter during Run04 for the extended range of the momentum transfers $-t$. The absolute scale was normalized against hydrogen polarimeter results in Run04. The curves are the model predictions(12) of with and without the spin-flip amplitude fitted to the data. The kinematic range $0.009 \leq -t \leq 0.023$ $(\mathrm{GeV/c})^2$ used for actual polarization measurements is indicated by the arrow.

## 2. EXPERIMENTAL APPARATUS

### 2.1. *Polarized Proton Beam at RHIC*

The polarized proton beam was injected to the RHIC storage rings at the energy of 24.3 GeV and was accelerated up to 100 GeV in the RHIC. The accelerated beam was stored in the ring for typically 6 to 7 hours and stores are distinguished by an unique RHIC fill number. Each RHIC ring was loaded with up to 112 bunches with alternating spin directions and with consecutive eight missing bunches at the end of the bunch train, used to abort the beam (abort gap). RHIC is operated with the revolution frequency of 78 kHz and bunches are spaced by 106 ns apart. The typical intensity is $10^{11}$ protons per bunch. The longitudinal distribution of the beam bunch is about 1.5 ns in $1\sigma$ and it limits the time-of-flight resolution of the single arm detection of the pC polarimeter.

The polarized beam becomes increasingly difficult to maintain the magnitude of the polarization with increasing energy due to the increased density and strength of the spin resonances. The Siberian snakes(4) in each ring rotate the spin vector by 180° with respect to a horizontal axis. The stable spin direction remains unperturbed at all times as long as the spin rotation from the Siberian snake is much larger than the spin rotation due to the resonance driving fields. Thus the beam polarization is preserved during acceleration. The polarization spin vector for each bunch was selected at the polarized $H^-$ source(13), and it is alternated from bunch to another bunch following a prefixed spin pattern.

2.2. *Target System And Detectors*

Carbon polarimeters consisted of carbon targets mounted on actuator systems and six silicon strip detectors. Detectors and targets are all installed in a vacuum scattering chamber as seen in Fig. 2. The photograph shows the scattering chambers of the blue and yellow polarimeters mounted on the blue and yellow ring beam pipes, respectively.

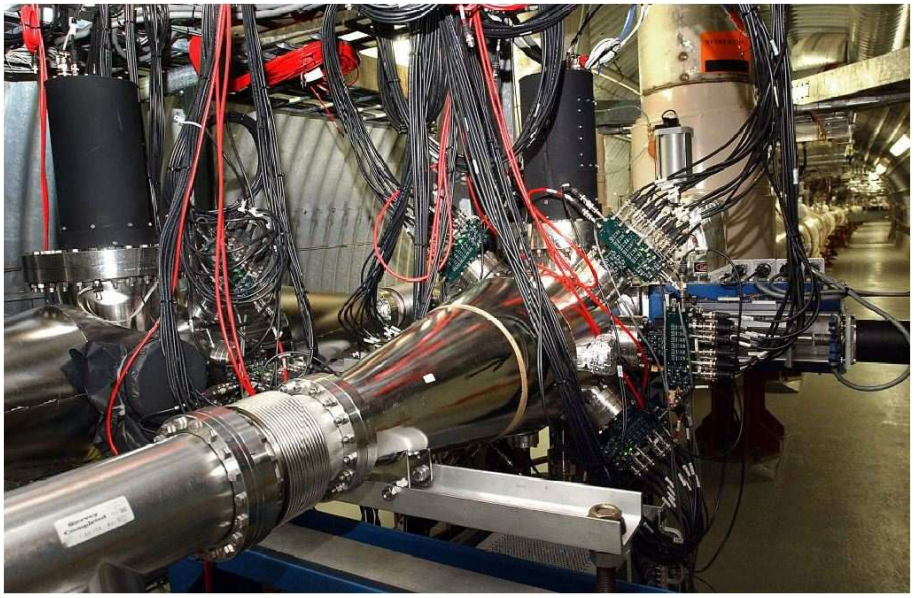

Fig. 2. The photograph shows the scattering chambers of the blue and yellow polarimeters mounted on the blue and yellow ring beam pipes, respectively.

Very thin carbon ribbon targets have been developed at Indiana University Cyclotron Facility(14). The targets were made by vacuum evaporation-condensation onto smooth glass substrates. A typical target is 2.5 cm long, 6 $\sim$ 8 $\mu$g/cm$^2$ thick and 10 $\sim$ 20 $\mu$m wide, and was glued on an open side of the "C"-shaped target folder frame as shown in Fig. 3. The targets are normally kept away from the beam line and it inserted into the beam only when the polarization measurement is executed, with a choice of one of the 6 vertical and 4 horizontal targets for Run06 as seen in the Fig. 3. Two stepping motors were used for each (vertical, horizontal) target assembly to drive a linear motion to move the whole assembly in and a rotary motion to pivot the desired target into the beam. The target position is monitored during a measurement, and is acquired into the data stream for the beam profile analysis. The target holder is capable of holding multiple targets simultaneously due to the short life time of the thin target against the radiation damage. The target lasted in about one week on average and the pre-mounted spare target was used without breaking the vacuum to replace the broken one.

Six silicon strip detectors manufactured by the Instrumental Division at BNL were mounted in a vacuum chamber at azimuthal angles of 90 and $\pm$45 degrees in both left

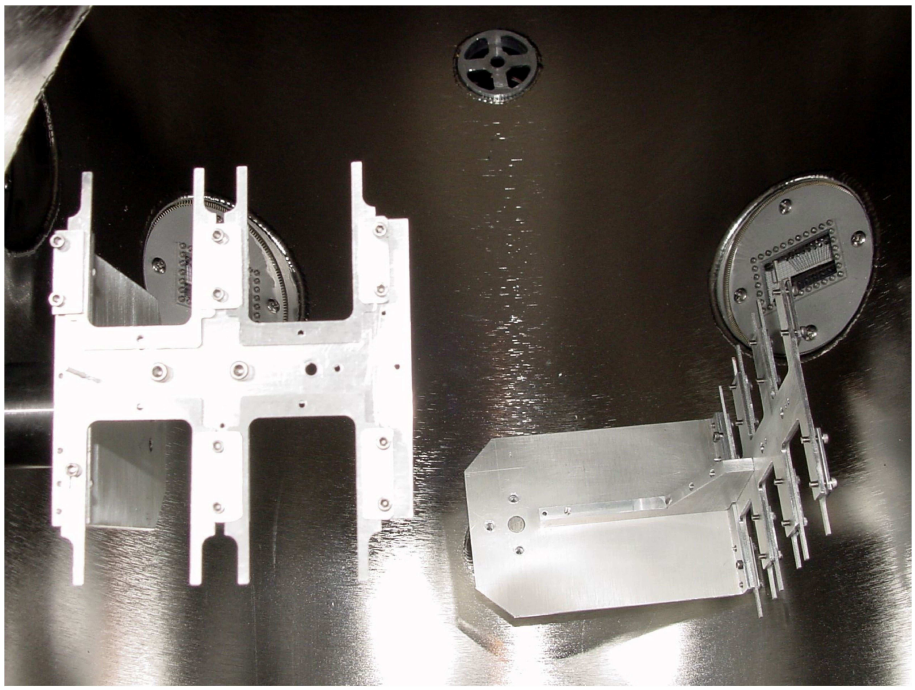

Fig. 3. The horizontal and vertical target folders viewed from the top of the scattering chamber. The beam goes from the bottom to the top of the photograph. Carbon targets are invisible in the photograph due to their thinness.

and right sides of the beam line [6] . A schematic drawing is shown in Fig. 4. The detector has $10 \times 24$ mm$^2$ total active area, divided into 12 strips of 10 mm $\times$ 2 mm as shown in the Fig. 5. The segmented axis of the detectors are oriented to the azimuthal direction, so there is no segmentation of the detectors in the beam direction. Thus the present setup do not have any sensitivity to the scattering angle of the recoil carbon ions within the acceptance, while the advantage is that the events are evenly distributed into all 12 strips. The thickness of the detector is 400 $\mu$m, fully depleted with the operation bias voltage of 100 to 150 V. Strips are made by the boron implantation p+-doping to a depth of 250 nm on the n-type Si bulk on the side facing the target. The right panel in Fig. 6 illustrates the cross section of the silicon detector. The distance from target to the silicon detectors was optimized to 18.0 cm. It is constrained by the travel time of the slowest (a few hundred keV) carbon ion to detectors before the next reaction by a consecutive bunch crossing takes place in 106 ns. Thus the elastic carbon events are secured from possible interference with the relativistic prompt backgrounds.

[6] The frame structure of the horizontal targets partially interferes with the acceptance of the 90° detectors. These 90° detectors were therefore excluded from the polarization analysis whenever the data were taken with horizontal targets.

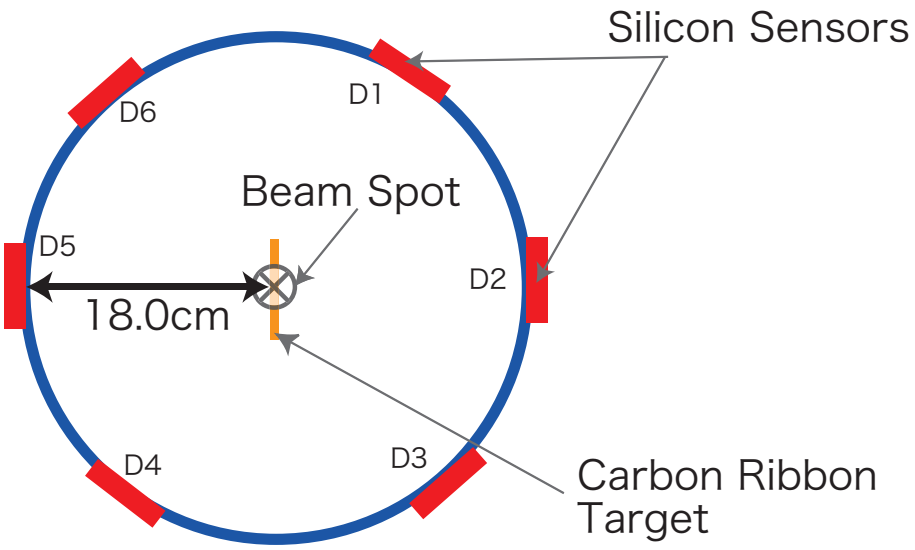


Fig. 4. A cross section of the RHIC pC-polarimeter setup. Silicon strip detectors are aligned 45°, 90°, and 135° azimuthally in both left and right sides of the beam direction. The beam points into the figure perpendicularly.

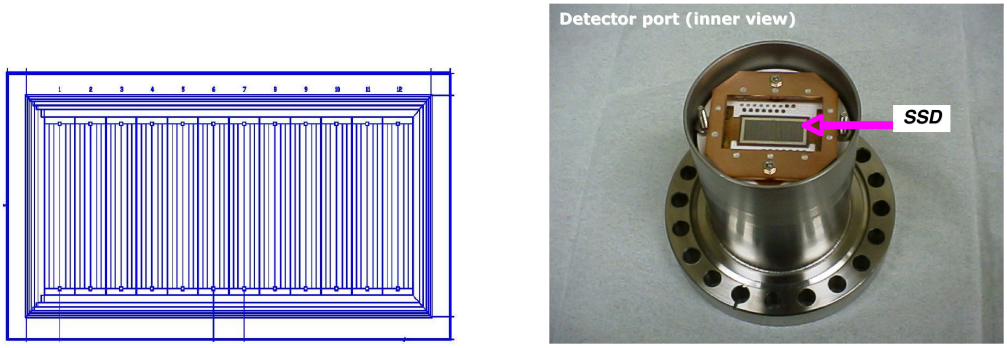


Fig. 5. (Left) The mechanical drawing of the silicon strip detector. Each detector is segmented into 12 strips with 2mm pitch. (Right) The silicon detector mounted on the support structure attached on a flange.

### 2.3. *Readout Electronics, Data Acquisition and Online Polarization*

If the dead time induced by the a read-out system correlated with the polarization sign change, it drives the polarization measurement into uncontrollable false asymmetries. One of the critical part of the pC polarimeter is thus a very fast (dead-timeless) DAQ system. Such system was built based on the fast waveform digitizer(16) (WFD) modules developed at Yale University. Signals from Si strip detectors are preamplified, transferred and shaped to obtain short (40ns FWHM) pulses with the amplitude proportional to the charge deposited in the detector. The pulse shapes are then digitized at the equivalent frequency of 420 MHz and analyzed inside the WFD modules, providing the recoil carbon deposited energy and time-of-flight. The events are then filtered through look up tables

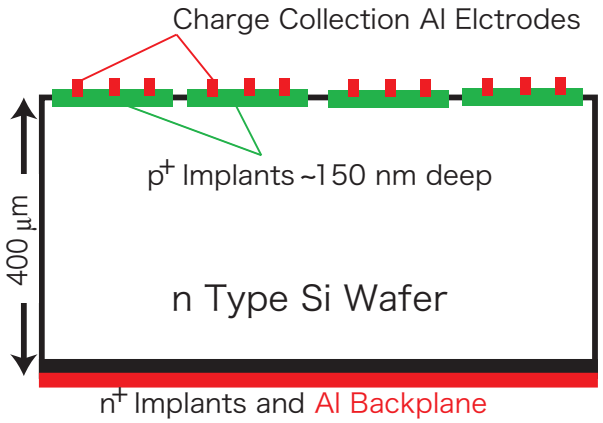


Fig. 6. The cross section of the silicon sensor.

(LUT), checking the kinematic correspondence between the obtained values for carbon identification. The selected events are used to increment scalers and histograms in the modules, and can be stored in the on-board memory. Shown in Fig. 7 is the typical kinematic correlation plot identifies elastic carbon events and backgrounds. The vertical and horizontal axes represent the time-of-flight and the kinetic energy reconstructed based on the time offset $t_0$ and an effective dead-layer thickness $x_{\rm dl}$ table used in online. The details of $t_0$ and $x_{\rm dl}$ are discussed in section 3.2. The online event selection was done in a wider range than that of the offline analysis, i.e. typically $\pm 15$ ns in time-of-flight and the deposited (measured) energy of $360 \sim 1100$ keV as shown in the solid curves in the figure.

The main advantage of such an approach is that there is no data transfer to the host computer during a data taking run, which makes the system true dead-timeless. The analyzing part is capable of processing of one event per RHIC bunch crossing period (106ns) resulting in maximum of $\approx 10^7/s$ events per channel.

The WFD is a CAMAC module hosting 4 independent channels as shown in Fig. 8 with common storage SDRAM (64 MByte) and CAMAC control circuity. In each channel the input signal is split into three, two of which are delayed 1/3 and 2/3 of the ADC digitization period. Three 8-bit ADCs synchronously start conversions at 140 MHz resulting in triple equivalent digitization frequency. All the waveform analysis is done inside the Vertex-E Xilinx FPGA chip(17) at 70 MHz clock frequency. The analysis algorithm is rather specific since it has to process every 6 waveform points in parallel (the FPGA clock is only 1/6 of the digitization frequency).

The block diagram of the analyzing circuits in the FPGA is shown in Fig. 9. The input signal passes through a digital filter for noise reduction and partial compensation for different amplifications of delayed sub-channels. A level trigger is used to determine the presence of a significant signal in a particular bunch crossing period, and if the signal is not detected, the ADC values are used for the baseline calculations. The baseline is determined individually for all three sub-channels to compensate for different amplifier offsets and is averaged over the 16 latest bunch crossing periods with no significant signal. The baseline is then subtracted and the signal is stored in FIFO, from which it can be directly read out as a waveform or taken for further analysis.

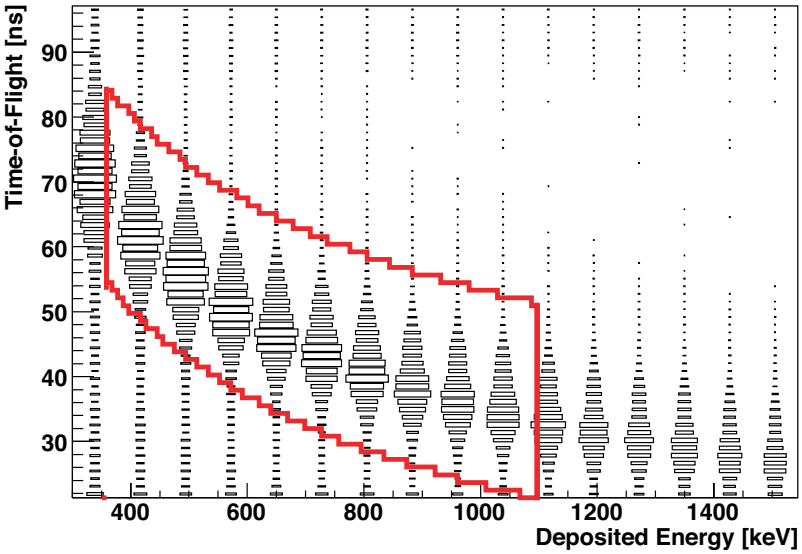


Fig. 7. The typical kinematic correlation plot observed in the online scaler mode. The vertical and horizontal axes represent time-of-flight and the deposited kinetic energy. Events surrounded by the red curves are selected events as the elastic recoil carbon events in online.

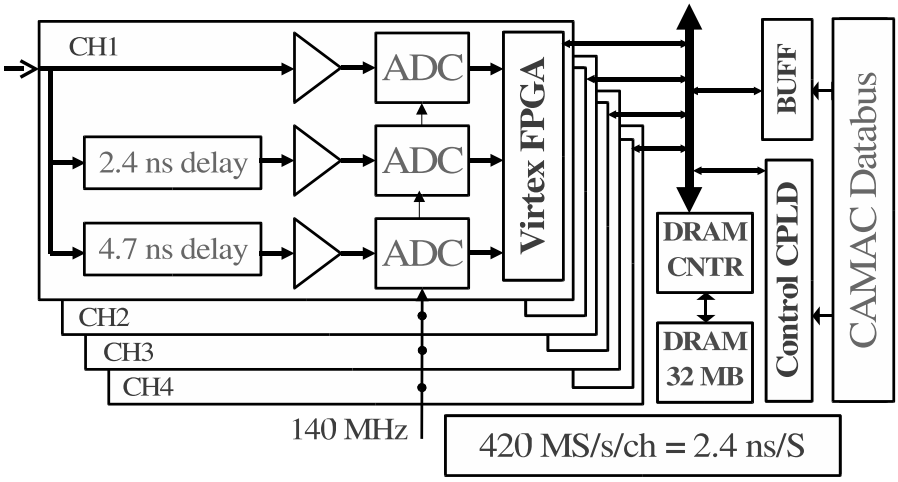


Fig. 8. A block diagram of the wave form digitizer.

The analysis is of the conveyor type and takes up to 5 stages, each stage corresponding to a sequential bunch crossing. On the first stage the whole waveform is used to define the signal amplitude (maximum), integral and time at maximum. The second stage implements 1/4 constant fraction discriminator (CFD) based on the amplitude value defined at the first stage. The CFD time and amplitude is then used to filter the event through a LUT, which is preprogrammed to account for energy-TOF correlation, specific for carbon

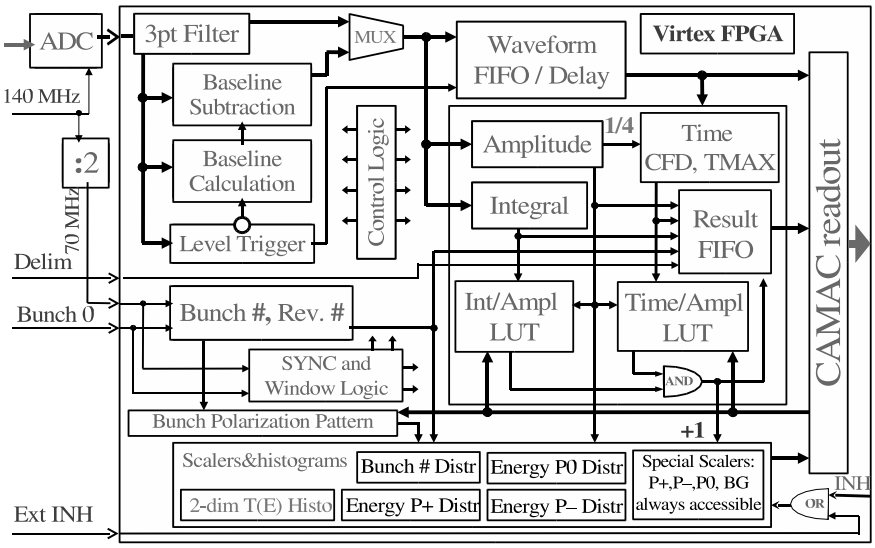


Fig. 9. A block diagram of the wave form digitizer per channel.

ions. Another LUT is used to compare the amplitude and integral values, which deviate from proportionality in case of two particles arriving within one bunch crossing. If both LUTs report positive result, all signal parameters are stored in the result FIFO and used to fill the on-board histograms. The FPGA keeps track of the bunch and revolution numbers, as well as of the bunch polarization pattern, which allows a variety of histograms including distributions of the energy (polarization sorted) and bunch number and 2D time-amplitude histograms. Their contents can be read out after the data taking and is sufficient for beam polarization determination in online. Yet for better understanding in offline analysis and debugging purposes the signal parameters from the result, FIFO can be transferred to the on-board storage memory, limiting the maximum event rate to $3 \cdot 10^6$ s$^{-1}$ per channel.

## 3. CALIBRATION AND ENERGY CORRECTION

### 3.1. *Energy Calibration*

The energy calibration of the silicon detectors is performed using an $\alpha$ source (241Am, (85%), 5.443MeV (12%)). The sources were mounted on the detector flanges and shine detectors on the opposite side of the beam. Dedicated calibration runs were executed several times throughout Run06 and typically very minor gain changes were observed for all the strips. The gain factor was determined from the mean of the Gaussian fit to the ADC distribution of $\alpha$ events strip by strip basis. Since the kinetic energy of the $\alpha$ is more than factor of 5 larger than the maximum Carbon energy used for regular polarization measurements, the signal output for the calibration was attenuated by 5 in order to accommodate it within a dynamic range of the ADC. About 1000 $\sim$ 1200 events are accumulated per strip. The resulting precision to determine the peak position is less than 0.1%, which is negligibly small compared to other uncertainties.

3.2. *Effective Dead-Layer and Energy Correction*

The $\alpha$ calibration, however, does not effectively probe the surface region of the detectors where the sub-MeV carbon ions stop. These low energy carbon ions entering the silicon detector penetrate the p+ doping layer (dead-layer [7]) first, and then enter the sensitive part of the detector, stopping at a depth of $< 1.3\mu$m. The energy loss of the carbon in the dead-layer is energy dependent and can be described by a known function of energy(15). This energy loss is a significant fraction of the carbon energy, for example, 30% for 400 keV carbon in dead-layer thickness of 50 $\mu$g/cm$^2$. In addition to this energy loss, the charge collection near the surface dead-layer can be affected by radiation damage. It has been unsuccessful to separate whether a change in the detector response either comes from a changing charge collection or from energy-dependent energy loss in the dead-layer. We consider the net energy correction, due to both the dead-layer and reduced charge collection near the surface, as a varying dead-layer thickness with the energy-dependent energy loss. As illustrated in Fig. 10, a realistic smooth transition of the efficiency between the dead-layer and fully efficient charge collection region (solid line) was treated as discrete transition (dashed line) introducing *"effective"* dead-layer $x_{\rm dl}$. The effective dead-layer thickness is determined empirically through a fit to the kinematical correlation of measured time-of-flight and kinetic energy correlation for carbon recoils.

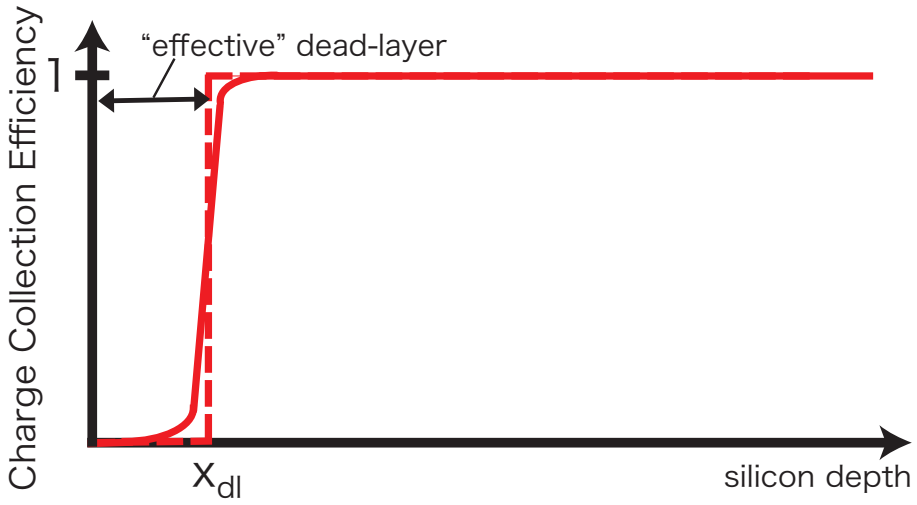


Fig. 10. The intuitive image of the charge collection efficiency as a function of the depth of the silicon detector. Solid line images realistic charge collection efficiency function whereas the dashed line represents *"effective"* dead-layer introduced in the main document.

Shown in Fig.11 is an example of the fit using the non-relativistic kinematic formula,

$$E = E_{\rm meas} + E_{\rm loss}(x_{\rm dl}, E) = \frac{1}{2} \cdot M \cdot \frac{L^2}{(t_{\rm meas} + t_0)^2} \qquad (2)$$

[7] The anticipated thickness calculated from p+ doping depth 250 nm is 250 nm $\times$ 2.33 g/cm$^3$ $\approx$ 58.3$\mu$g/cm$^2$, which is reasonably consistent with the effective dead-layer thickness observed at the beginning of Run06 before silicon detectors were damaged by radiation.

where $M$, $L$, $t_{\rm meas}$ and $E_{\rm meas}$ are the mass, the flight path length, the measured time-of-flight, and the energy of the recoil carbon ion, respectively. A time offset $t_0$ and the effective thickness of the dead-layer $x_{\rm dl}$ were set as free parameters. The energy correction $E_{\rm loss}$ has dependency on the $x_{\rm dl}$ and the incident energy of the carbon ions $E$. The time-of-flight $t_{\rm tof}$ is given as $t_{\rm tof} = t_{\rm meas} + t_0$. Details of the parameterization of $E_{\rm loss}(x_{\rm dl}, E)$ in the silicon surface are discussed in Appendix I. The empirical fit was applied to all polarization measurements during physics stores and evaluated the effective dead-layer thickness for each measurement independently to trace the stability.

The data in Fig.11 is from a typical polarization measurement, but the events are plotted only 1/10 of full events for display purpose. Horizontal axis shows the measured energy $E_{\rm meas}$ in [keV] (observed ADC multiplied by the gain factor), whereas the vertical axis is the measured TDC $t_{\rm meas}$ in the unit of [ns] (not corrected for $t_0$). The curve with finite band in the middle of the plot represents for carbon ion events. Small, but finite $\alpha$ backgrounds come from inelastic reaction distribute around small time-of-flight and measured energy region. Relativistic backgrounds such as prompt photons and pions, etc should appear around the time-of-flight of zero region. The timing window gate was tuned to exclude these fast particles in order to prevent the DAQ live-time to be over killed.

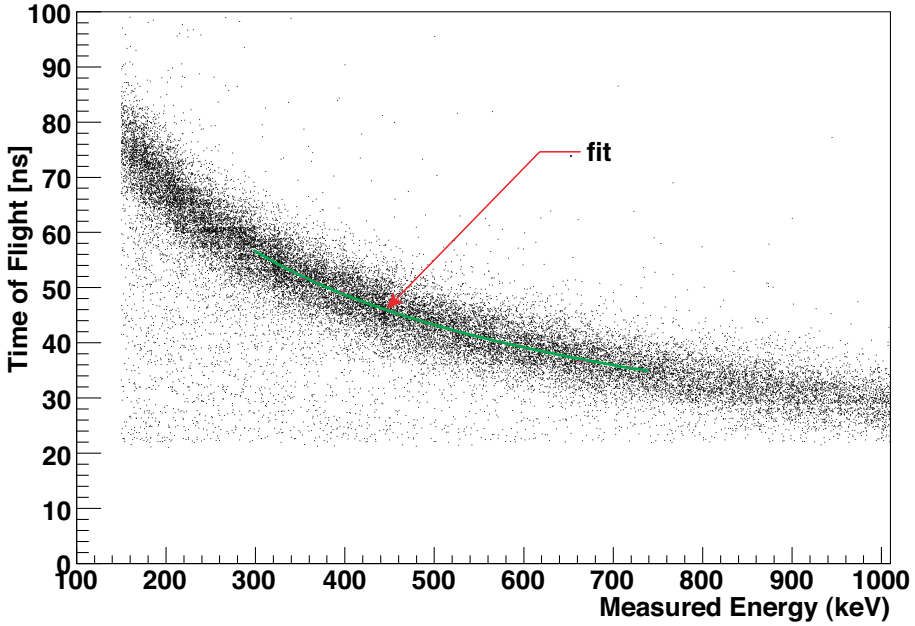


Fig. 11. An example of the kinematical fit with the energy correction (effective dead-layer thickness $x_{\rm dl}$) and time offset $t_0$ set as free parameters. The best fit curve on data is drawn. Fitting range $306 \leq E_{\rm meas} \leq 742$ keV corresponds to the standard kinetic energy range $400 \leq E \leq 900$ keV in case of the effective dead-layer $x_{\rm dl} = 40 \mu{\rm g/cm}^2$.

Although the data cover broader energy range, events within $400 \leq E \leq 900$ keV were selected as inputs to the dead-layer fit. The range is consistent with the event selection made for the polarization calculation and was always used for all Run06 measurement. Note any incorrect energy correction should be absorbed by the normalization against

the absolute polarization measurement by the H-Jet polarimeter. Therefore it shouldn't appear in the polarization measured by the pC polarimeter at least for the first order once they are properly normalized. Thus only relative stability from one measurement to another matters as a systematic uncertainty of pC polarimeters. Shown in Fig. 12 are the estimated effective dead-layer thickness averaged over all active strips per measurement, $\overline{x_{\rm dl}}$, plotted as a function of the fill number. The error is the average deviation of individual strip's $x_{\rm dl}$ from the strip total average $\overline{x_{\rm dl}}$. Each data point represents one measurement performed at the stored beam energy in blue (left) and yellow (right) rings. Data points are plotted only for measurements performed during the physics stores. As can be seen from the figure, the resulting effective thicknesses of dead-layers are not constant and change from measurement to measurement. A shallow rises ($\sim 8$ $\mu$g/cm$^2$) in the thickness of effective dead-layer are observed in both blue and yellow polarimeters. Presumably they are caused by the deteriorated charge collection efficiency near surface area due to accumulated radiation damage. A stability error was estimated to be $\pm 4\mu$g/cm$^2$ which was translated to the relative polarization uncertainty of $\pm 2.4\%$.

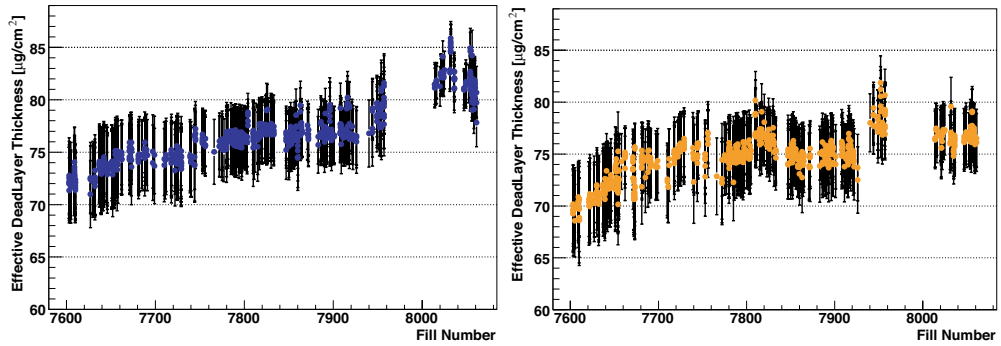


Fig. 12. Stability of the effective dead-layer thickness averaged over all active strips plotted as a function of fill number for the blue (left) and the yellow (right) polarimeters, respectively.

## 4. EVENT SELECTION

Shown in the Fig. 13 is the typical time-of-flight and the kinetic energy plot reconstructed using the best parameters of the effective dead-layer fit. Solid curve represents $3\sigma$ cut on the invariant mass as demonstrated by dashed lines in Fig.14. The background tail towards smaller mass region is primarily comes from inelastic $\alpha$s whose invariant mass does not necessarily be reconstructed at the right $\alpha$ mass because the energy correction in the effective dead-layer was calculated assuming the carbon ion. A contamination of the $\alpha$ backgrounds underneath the carbon invariant mass peak is typically much less than 1% within $\pm 3\sigma$ from the nominal carbon mass position. Elastic carbon ions are observed typically $200 \sim 300$ thousand events per strip with in $|\Delta M| < 3\sigma$ mass cuts. About 50% of accumulated events from raw data were dropped after the energy ($400 \leq E \leq 900$ ) and the $|\Delta M| < 3\sigma$ cuts were applied.

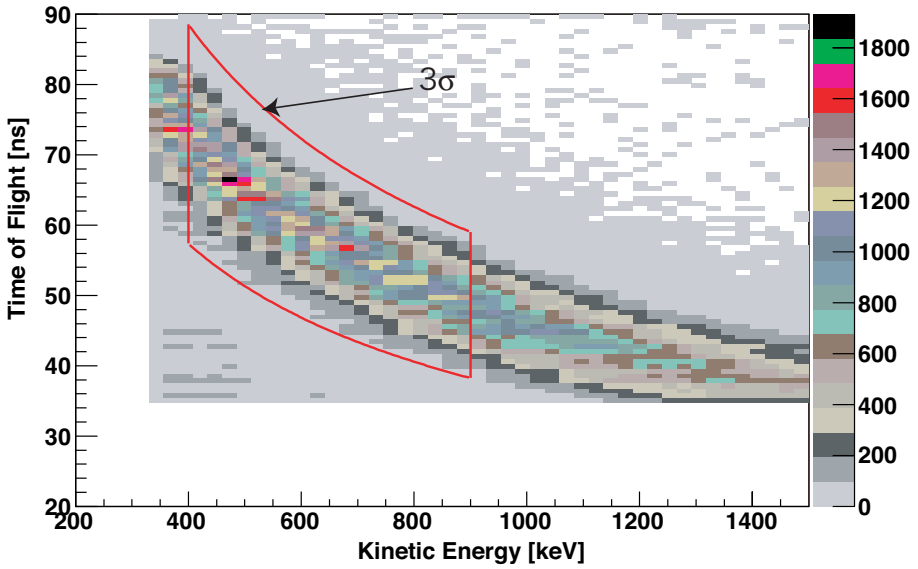


Fig. 13. Time of flight and reconstructed kinetic energy correlation plot after the energy correction. Solid curve distinguishes events within $3\sigma$ from carbon mass in the invariant mass distribution and the energy range $400 \leq E \leq 900$ keV.

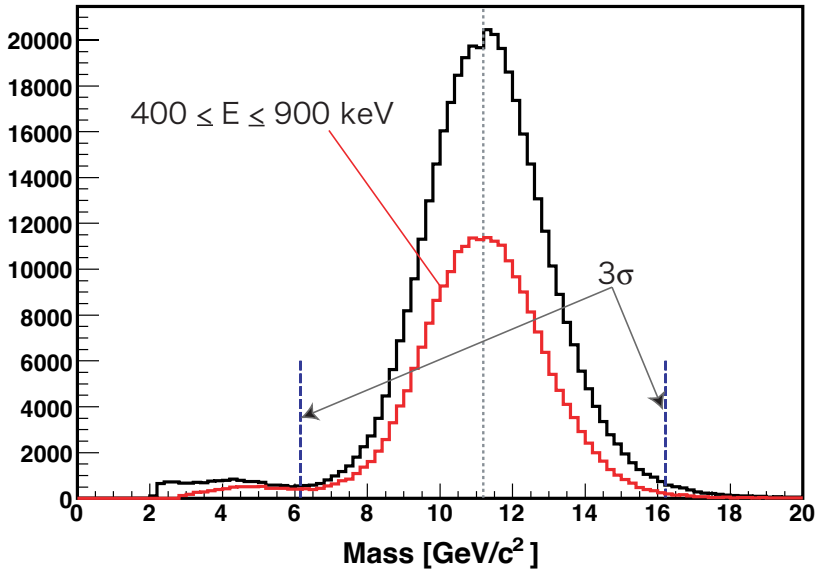


Fig. 14. A typical reconstructed invariant mass distribution. The red histogram shows the invariant mass for the events $400 \leq E \leq 900$ keV while black histogram shows all events in a given strip. Dashed line represents $3\sigma$ from the nominal carbon mass (dotted line).

## 5. ASYMMETRY AND POLARIZATION

### 5.1. *Bunch By Bunch Asymmetry*

The beam in RHIC has bunch structure as described in Section 2.1 and bunches can be loaded up to the maximum of 112. Each beam in bunches are polarized either positive or negative following prefixed spin patterns. Since every accumulated events are tagged by the bunch ID in the data stream, the asymmetries can be calculated for every bunches separately. This is the good check of the consistencies between the polarizations from one bunch to another.

The asymmetry for a given bunch *bid* is defined as follows:

$$A_{bid} = \frac{N^{\rm L}_{bid} - R^{\rm lumi}_{bid} N^{\rm R}_{bid}}{N^{\rm L}_{bid} + R^{\rm lumi}_{bid} N^{\rm R}_{bid}} \tag{3}$$

where *bid* stands for the bunch ID, $N^{\rm L}_{bid}$ ($N^{\rm R}_{bid}$) is the number of events (after event selection cuts) in the left (right) detector of the bunch ID=*bid*. The luminosity of the bunch *bid* is calculated by taking sum of $N^{\rm L}_{bid}$ and $N^{\rm R}_{bid}$,

$$R^{\rm lumi}_{bid} = \frac{\sum_{bid}^{112} N^{\rm L}_{l}}{\sum_{bid}^{112} N^{\rm R}_{l}}. \tag{4}$$

The physical asymmetry of vertically polarized beam can be measured by taking the left-right combinations using detectors mounted at azimuthal angle of 90 degrees (D2,D5) as shown in the top-left panel in Fig. 15. This combination is named X90 combination. Using detectors combination mounted at $\pm 45$ and $\pm 135$ degrees, the physics asymmetry can be also measured as shown as a X45 combination in the top-right panel in Fig. 15. The independent measurement of the raw asymmetry is quite important to monitor the systematics of the detector system. Although the sensitivity of X45 combination to the vertical polarization is suppressed by $\sqrt{2}$ than that of X90, statistical abundance compensates it by combining events in four detectors (D1+D3,D4+D6). Taking advantage of the possible combinations can be made out of 6 detectors, forbidden asymmetries with respect to the vertical spin vector can be evaluated. For instance, finite asymmetry should be observed by the combinations of (D1+D6,D3+D4), named Y45, only when the spin vector has a radial component as shown in the bottom-left panel. In other words the Y45 combination supposed to be zero when the spin vector is pointing perfectly vertical. As shown in the bottom-right panel, the observation of the finite asymmetry in the cross combination (D1+D4,D3+D6) immediately indicates systematic anomaly in a measurement.

Shown in the Fig. 16 are the raw asymmetries of X90 (top left), X45 (top right), and Y45 (bottom left) plotted as a function of bunch number. Red and blue solid circles represent positively and negatively polarized bunches based on the prefixed spin pattern. In both physics asymmetries X90 and X45, red and blue solid circles are well consistent to each other and indicates finite non-zero asymmetries. On the contrary, blue and red circles are distributing around zero in Y45 asymmetries. In this typical good example, all asymmetry combinations show $\chi^2$ of around 1 to the mean for both positive(+) and negative(-) bunches as printed in the top and bottom corners of asymmetry plots in Fig. 16.

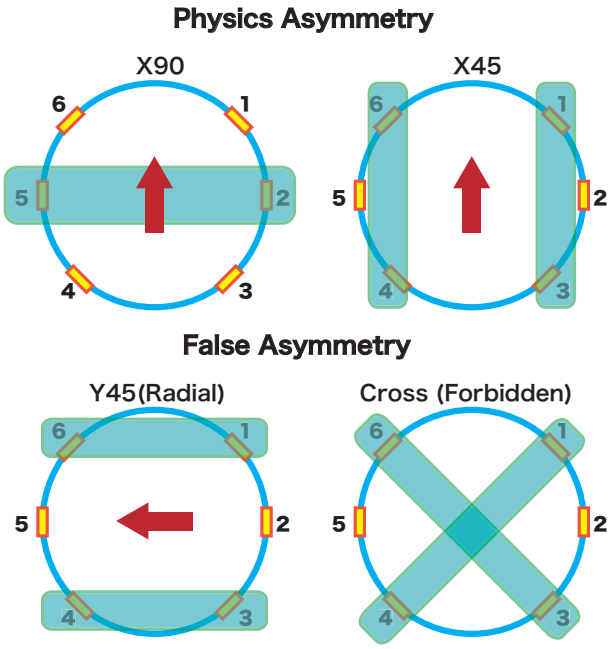


Fig. 15. Detector combinations which form physics (top) and false (bottom) asymmetries.

Bottom right panel shows so called specific luminosity which is calculated by number of events within the kinematic cuts per bunch divided by the bunch beam intensity measured by the wall current monitor(18). Since the events per bunch are normalized by the beam intensity, any deviation of a data point from other bunches suggests irregular emittance of that particular bunch or otherwise direct indication of the anomaly in the detection system, e.g. the cross talk of events between bunches. Such anomalous bunches were barely observed throughout Run06 measurements, however once be found, they are excluded from the analysis. We will discuss it more in Section 6.1.

### 5.2. *Average* $A_{\rm N}$

Carbon events which passed kinematic cuts ($|\Delta M| \leq 3\sigma$ and $400 \leq E \leq 900$ keV) were then integrated over the energy range. As it will be discussed in details in Section 5.3, the polarization is extracted through a sine modulation fit on strip asymmetries. The observed asymmetries were divided by the average $\overline{A_{\rm N}}$ to be translated to polarizations. The $\overline{A_{\rm N}}$ is the average analyzing power within the energy range of the present event selection. It is calculated by the averaging energy dependent $A_{\rm N}(E)$ weighted by the yields $Y[i]$ of the $i$th bin in the energy spectrum. $E_i$ is the $i$th bin of the energy $E$ spectrum:

$$\overline{A_{\rm N}} = \frac{\sum_i^N A_{\rm N}(E_i) \times Y[i]}{\sum_i^N Y[i]} \tag{5}$$

where $A_{\rm N}(E_i)$ is the $A_{\rm N}$ at the energy bin $E_i$ and $N$ is the total number of bins in the energy spectrum. Shown in Fig.17 is the typical energy spectrum of the carbon

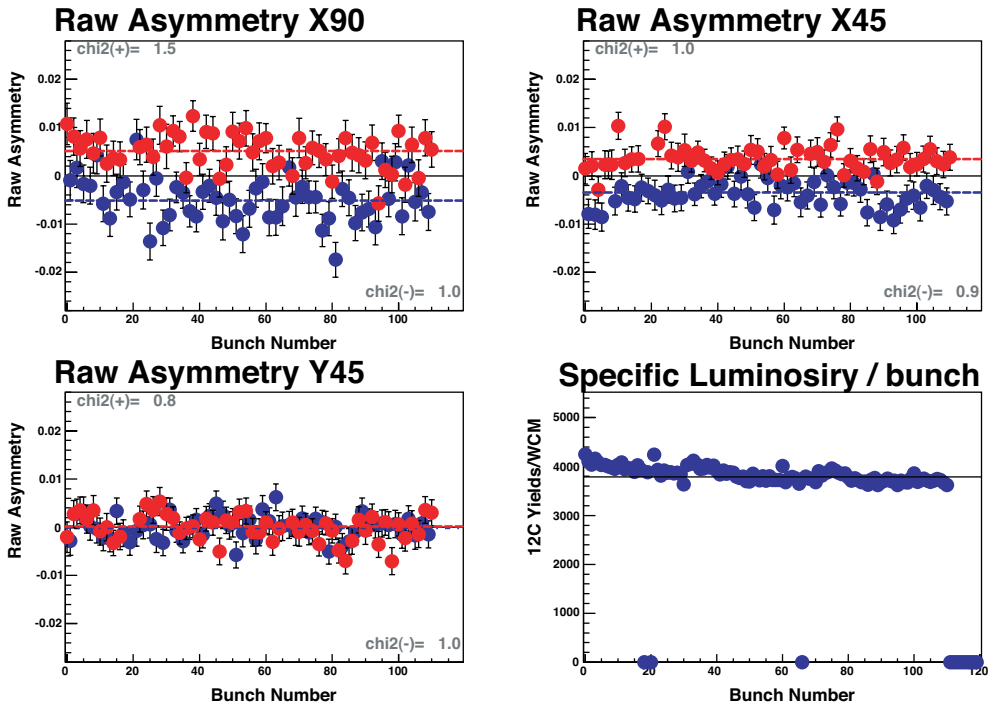


Fig. 16. Typical example of bunch asymmetries for three different combinations of detectors, i.e. X90 (top left), X45 (top right) and Y45 (bottom left). Red and blue solid circles represent raw asymmetries of positively and negatively polarized bunches, respectively. The $\chi^2$ with respect to the mean (dashed lines) are printed at the top and bottom corners of these panels. The bottom-right panel shows the specific luminosity distribution as a function of bunch number.

events combined for all active strips after the kinematic cuts. The curve is a model prediction with hadronic spin flip(12) of $A_{\rm N}(E)$ as plotted in Fig. 1, scaled by the Run04 data. The momentum transfer $-t$ and the kinetic energy of recoil carbon are related nonrelativisticly: $E = -2Mt$, where $M$ is the nominal carbon mass.

### 5.3. $\sin(\phi)$ *modulation fit*

The polarization of each pC-polarimeter measurement is calculated based on the strip asymmetries, combining all individual bunch asymmetries. The asymmetry of strip $i$ is calculated using the number of elastic carbon events after the kinematic cuts for all positive bunches $N_i^+$ and negative bunches $N_i^-$ in strip $i$:

$$A_i = \frac{N_i^+ - R_i N_i^-}{N_i^+ + R_i N_i^-} \tag{6}$$

where $i$ runs for active strips up to 72. The luminosity ratio $R_i$ for the strip $i$ is defined

$$R_i = \frac{\sum_{j\neq i,37-i,36+i,72-i}^{72} N_j^+}{\sum_{j\neq i,37-i,36+i,72-i}^{72} N_j^-}. \tag{7}$$

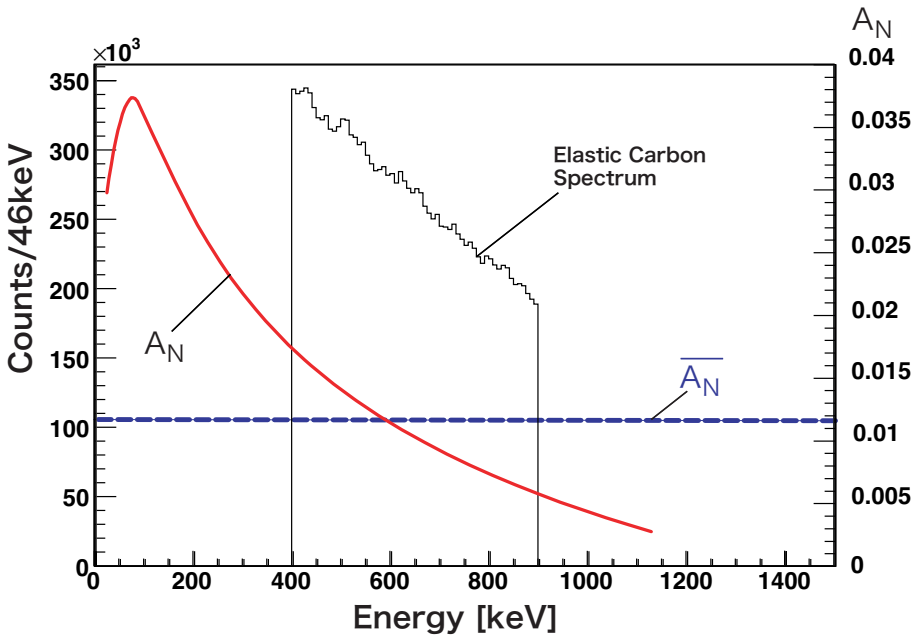


Fig. 17. The typical energy spectrum of the carbon events combined all active strips after the kinematic cuts. The curve is a model prediction of $A_{\rm N}(E)$ scaled by the Run04 data. Dashed line shows the weighted average $\overline{A_{\rm N}}$.

In order to remove the bias effect from the strip $i$ for the luminosity calculation, the strip $i$ is excluded from the luminosity calculation. Also to avoid introducing false asymmetry comes from the geometrical acceptance effect by doing so, not only the strip locates diagonally opposite location, but also ones locate at cross geometries are excluded as well. Total of 4 strips thus were excluded from the luminosity calculation for the asymmetry calculation of a given strip.

Shown in Fig. 18 with solid circles are typical example of typical example of strip asymmetries $A_i$ divided by the $\overline{A_{\rm N}}$ plotted as a function of the azimuthal angle of each strip in the unit of radian. The coverage of the 2 mm strip width is translated to be 11 mrad in the azimuthal angle acceptance.

The strip polarizations are then fitted with the sine function:

$$P(\phi) = \frac{A_i}{\overline{A_{\rm N}}} = P \sin\phi \tag{8}$$

where $P$ is strip averaged polarization and $\phi$ is a radial spin vector, respectively and they were set as free parameters. The best fit result is drawn by the solid curve in the figure.

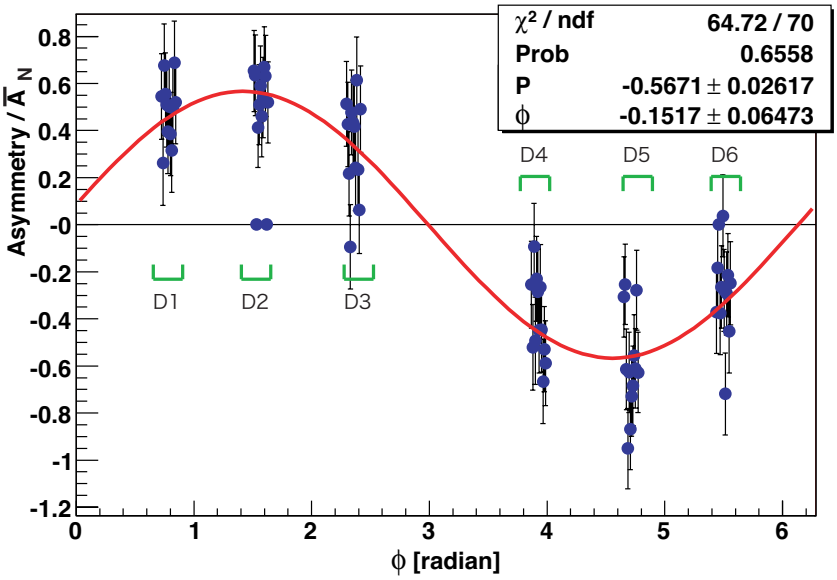


Fig. 18. The strip by strip polarization plotted as a function of the azimuthal angle (rad). The red curve represents the best fit to the data using the function (8) defined in the main text.

## 6. JET NORMALIZATION

### 6.1. *Data Selection*

Before comparison with the average polarization measured by the H-Jet polarimeter, the reliable data were selected through the quality assurance of the all data taken during H-Jet operation periods. It includes a) slope of the energy spectrum; b) strip by strip based anomaly check; c) bunch by bunch based anomaly check. The data have to satisfy following criteria to be reliable; 1) consistent number of events accumulated for all strips; 2) the invariant mass is reconstructed at the right position; 3) small correlation observed in the reconstructed mass position and the kinetic energy of recoil carbon ions; 4) the reconstructed mass peak has consistent width for all strips. Because there are total of 72 redundancies, strips are simply eliminated from the analysis if the number of strips which do not pass above criteria is small. Otherwise we dropped whole run from the good run list when the large fraction of strips behaved wrong. The item c) is the anomaly check on the bunch asymmetries as discussed in Section 5.1. Any bunches show asymmetry inconsistent more than $5\sigma$ from the average asymmetry of all bunches were excluded from the analysis. Similarly to the strip case, whole run was dropped from the good run list when more than a couple of bunches show anomalous asymmetries simultaneously.

### 6.2. *Polarization Profile*

The typical beam size at the 100 GeV at the location of pC polarimeters is around $1.5 \sim 2$ mm at FWHM, while the carbon ribbon target width is only $\lesssim 20\mu$m. Thus it measures only the polarization of the small portion of the beam intercepted by the target.

On the other hand, the FWHM of the H-Jet gas target is about 6 mm, wide enough to cover the whole beam spot size at IP12. Therefore what the H-Jet measures is averaged polarization over the beam profile. The intrinsic difference between pC and the H-Jet polarimeters is thus the coverage area of the finite transverse target beam spot size as illustrated in Fig. 19. Yet the measured polarization by pC-polarimeters can be directly comparable to what the H-Jet polarimeter measures and applicable to the experiments, only if there is no polarization profile in the beam. This is not the case in reality in fact the RHIC beam often show finite polarization profiles.

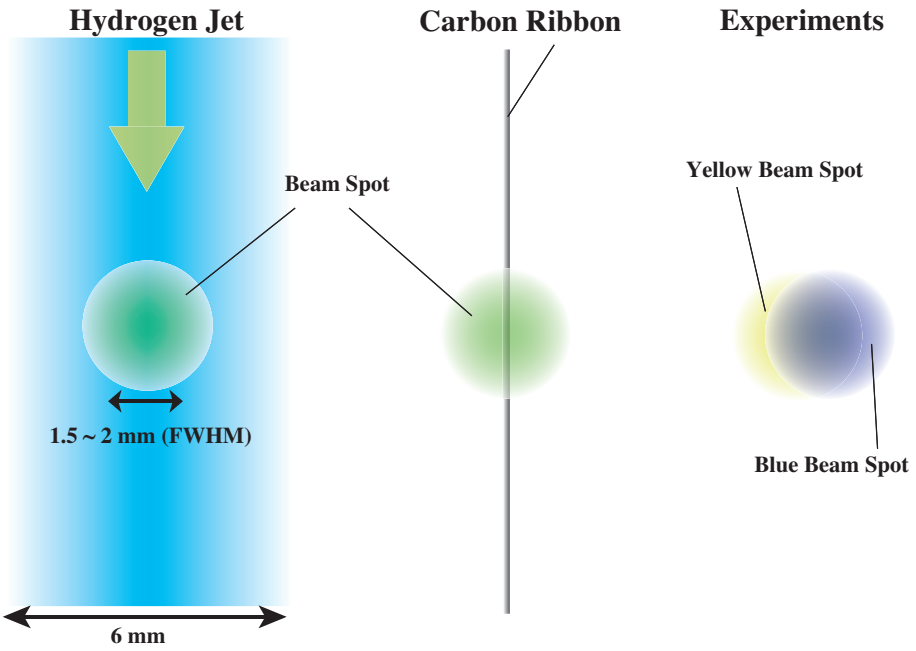


Fig. 19. Images of the area coverage difference of the target on the beam spot between the H-Jet (left) and proton-Carbon (middle) polarimeters and experiments (right).

Shown in Fig. 20 are the polarization (top) and intensity (bottom) profiles observed during one of a fill in the yellow ring during Run05. Each data point corresponds to an independent polarization measurement at a given target position with respect to the beam. Series of measurements were taken in every $\sim$ 0.5 mm step across the horizontal beam profile. Despite the event rate dropped so rapidly toward the edge of the beam, each measurement was accumulated constant statistics, i.e. $\sim$ 20 million events to define the both wings of the profile well. As figures demonstrate, both polarization and intensity profiles were well fit by the Gaussian shape. The strength of the profiles thus can be characterized by the resulting widths $\sigma$.

Two Gaussians of the beam intensity and the polarization profiles are given as a function of the target position $x$ ($x$ is the relative distance from the intensity peak, not absolute target position) :

$$\mathcal{I}(x) = e^{-\frac{x^2}{2\sigma_{\mathrm{I}}^2}} \tag{9}$$

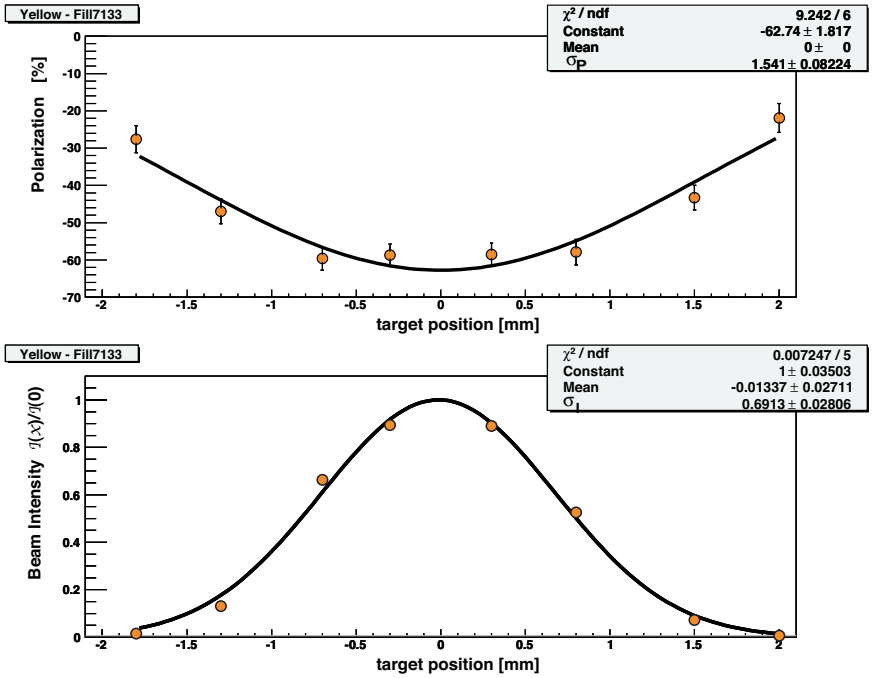


Fig. 20. The horizontal polarization (top) and the intensity (bottom) profiles of the yellow beam observed during Run05. The vertical axis of the intensity profile is calculated from the event rates normalized at the peak amplitude of the Gaussian fit. The horizontal axes are the relative target position in mm with respect to the beam center defined by the Gaussian fit on the intensity profile.

$$\mathcal{P}(x) = e^{-\frac{x^2}{2\sigma_{\rm P}^2}} \tag{10}$$

where $\mathcal{I}(x)$ and $\mathcal{P}(x)$ are the intensity and the polarization profiles normalized to be 1 at their peaks, and $\sigma_{\rm I}$ and $\sigma_{\rm p}$ are width of these profiles, respectively. There are also profiles in vertical direction, but it is averaged over for this case due to the usage of the vertical target. Eliminate $x$ from these equations, then we obtain

$$\mathcal{P} = \mathcal{I}^{\,r_{\rm x}} \tag{11}$$

where

$$r_{\rm x} = (\frac{\sigma_{\rm I}}{\sigma_{\rm P}})^2. \tag{12}$$

Since $\mathcal{I}$ and $\mathcal{P}$ are defined as the relative intensity and the polarization with respect to the peak, they run from 0 to 1. Thus Eq. 11 gives $\mathcal{P} = 1$ at the peak intensity $\mathcal{I} = 1$.

There were only three dedicated profile measurements performed as Fig. 20 throughout Run05. Such a poor knowledge of the polarization profile blew up the systematic uncertainty to normalize the polarization measured by pC polarimeters against that of the H-Jet polarimeter(10). As an improvement in Run06, the regular polarization measurements were performed by scanning the carbon wire target across the transverse beam profile. This is a different approach compared to fixed target position measurements in

Run05. This way the profile correction on the normalization process becomes unnecessary, because the pC polarimeter measures the profile averaged polarization just as H-Jet polarimeter measures. Scanning over horizontal (vertical) direction by vertical (horizontal) target during the measurement averages over scanning direction, while the vertical (horizontal) wire target automatically averages over the other vertical (horizontal) dimension. The scan was made with step size of several hundred $\mu$m across the beam intensity profile for constant intervals (typically a few seconds) at each target position. The interval at every target positions was kept constant on purpose so that the whole beam is properly represented. It should be noted that, this is different from the dedicated profile measurement as shown in Fig. 20, which was accumulated constant statistics (stayed longer towards edge) at each target position.

### 6.3. *Normalization*

The H-Jet polarimeter was operated for the blue and the yellow beams sequentially switching every a few days through Run06. We grouped these H-Jet operation periods and compared with the polarizations of pC polarimeters averaged over the corresponding periods. Whereas the H-Jet polarimeter was operated continuously throughout a fill, pC polarimeters take "snapshot" polarizations of the fill for multiple times (typically 4 or 5 times for 7 hours' fill). The H-Jet polarimeter measures polarization which is not only averaged over the transverse polarization profile, but also averaged over the over the fill (time). As a consequence, the measured polarization is automatically biased by the period while the beam intensity is high, simply because it triggers more events to the H-Jet polarimeter. On the other hand, each measurement of pC polarimeters was accumulated same statistics regardless of the beam intensity. Thus the average of polarization over a fill was calculated by taking weighted average over the beam intensity for pC polarimeters. Also the duration between one measurement to another measured in a same fill was taken into account in the weighted average so that each measurement represents the average polarization of that period properly. This is just to avoid the average polarization to be biased by some multiple measurements in a row.

Shown in Fig. 21 are the ratio of the average polarizations of pC and H-Jet polarimeters. Data points represent these polarization ratios for the several H-Jet operation periods as described at the beginning of this Section. Linear fits shown in solid lines give $\chi^2/d.o.f$ of 6.3/4 and 1.1/2 for the blue and the yellow average polarization ratios, respectively. Run06 absolute normalization scales $S = \overline{P_{\rm pC}^{\rm Run06}}/\overline{P_{\rm H-Jet}^{\rm Run06}}$ for pC polarimeters determined by the fit were 1.138$\pm$0.030 and 1.152$\pm$0.026 for the blue and yellow polarimeters, respectively. Errors are statistical only, which primarily come from the average polarizations measured by the H-Jet polarimeter. Normalization scales are consistent between the blue and yellow pC polarimeters within the statistical uncertainties.

## 7. POLARIZATION FOR EXPERIMENTS

### 7.1. *Run06 Polarization Profile*

The measured polarizations by pC polarimeters $P$ are now scaled by the normalization factors $S$ as derived in Section 6.3 and they are now all in absolute scale $\widetilde{P_{\rm pC}}$:

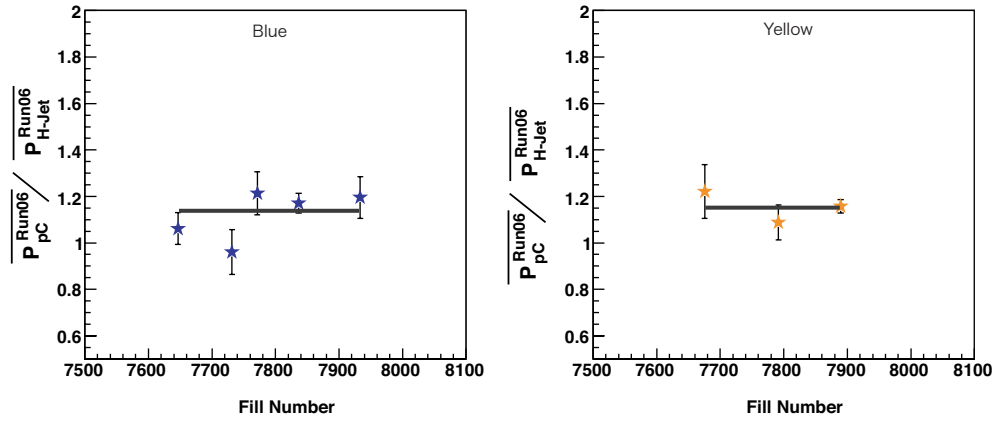


Fig. 21. The ratio of the average polarizations measured by the pC and the H-Jet polarimeters for several periods of the blue (left) and the yellow (right) beams. Solid lines are linear fits to data.

$$\widetilde{P_{\mathrm{pC}}} = \frac{P}{S}. \tag{13}$$

Yet the polarization profile correction is still necessary to translate the average polarization measured by the pC polarimeter to the polarization applied for the experiments whose polarization is weighted differently on the beam intensity profile, unlike the H-Jet polarimeter case. As illustrated in Fig. 19, under the assumption of the head on collision, the contribution of the polarization profile to the average polarization is weighted by the product of blue and yellow beam intensity profiles in experiments, whereas the average polarization obtained by the scan mode pC polarimeter measurements are only a single beam intensity profile weighted. The polarization profile correction is thus necessary to translate $\widetilde{P_{\mathrm{pC}}}$ to the adequate polarization for experiments.

The polarization profiles were evaluated empirically from Run06 data for all physics fills, individually. A typical fill lasted within 7 hours, and several polarization measurements using the pC-polarimeters were executed during the store in the scan mode as described previously. Each measurements are the convolution of a few seconds measurements at different transverse target positions across the beam. Shown in the Fig. 22 is a typical correlation between observed polarization and the relative beam intensity normalized by the maximum intensity at the center of the beam. The relative intensity in the horizontal axis corresponds to the relative distance of the target position to the beam center. Thus each data point represents a few second measurement at a given target position of the scan mode operation. All measurements during the fill are superposed in the plot assuming the profile do not change drastically within the fill. The measurements toward the edge of the beam (towards zero in horizontal axis) are low statistics, because of low rate. Shown in solid line is the best fit using Eq. 12 where $r_{\mathrm{x}}$ was set as a free

parameter. The fit was applied for the region $0.1 \leq \mathcal{I}/\mathcal{I}(0) \leq 1.0$.

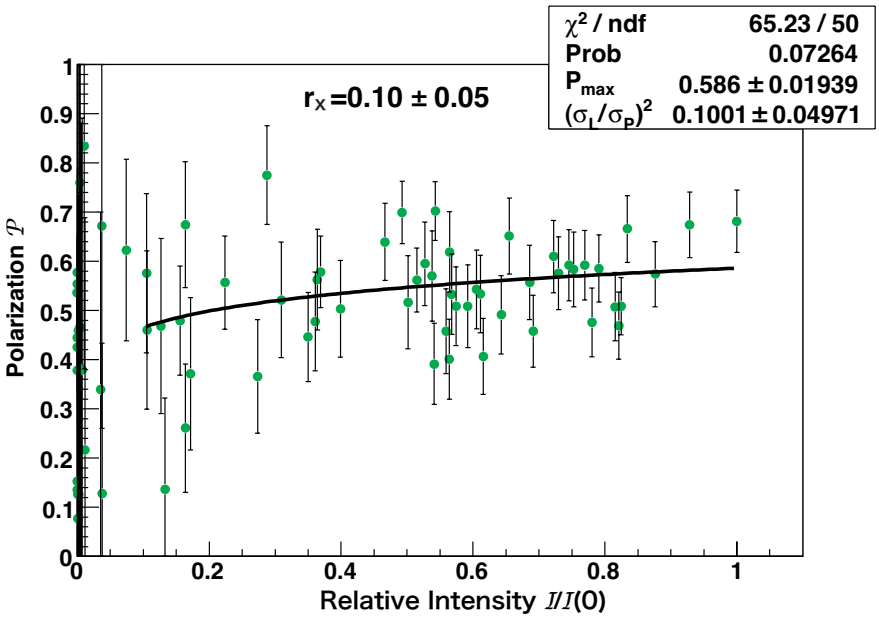


Fig. 22. A typical horizontal polarization profiles evaluated by several measurements in the same fill. The horizontal and vertical axis are relative intensity $\mathcal{I}/\mathcal{I}(0)$ and polarization $\mathcal{P}$, respectively. Solid curve is the best fit on data in the range of $0.1 \leq \mathcal{I}/\mathcal{I}(0) \leq 1.0$ using the function (11). $r_{\rm x}$ was set as a free parameter.

Shown in Fig. 23 are extracted polarization profiles (fill-averaged) for the horizontal $r_{\rm x}$ and vertical $r_{\rm y}$ directions for all physics stores at the beam energy of 100 GeV. The horizontal axis is the RHIC fill number. As can be seen in the figures, the observed $r_{\rm x}$ and $r_{\rm y}$ are consistent to each other between different fills. Thus we evaluate a global polarization profiles from averages for the blue and yellow beams for both horizontal and vertical directions, separately. Results are tabulated in Table. 1.

Table 1
The global polarization profiles for the blue and yellow beams in both horizontal and vertical directions, respectively.

| Beam | $r_{\rm x}$ | $r_{\rm y}$ |
|---|---|---|
| Blue | $0.071 \pm 0.005$ | $0.095 \pm 0.019$ |
| Yellow | $0.094 \pm 0.004$ | $0.078 \pm 0.024$ |

### 7.2. *Profile Correction*

In this section, the correction due to the polarization profile is calculated. The polarization measured by the pC-polarimeters $\widetilde{P_{\rm pC}}$ in the scan mode are correlated with the peak polarization at the beam center (in both horizontal and vertical wise) $P_{\rm peak}$:

$$\widetilde{P_{\rm pC}} = P_{\rm peak} \cdot C_{\rm 1X} \cdot C_{\rm 1Y} \tag{14}$$

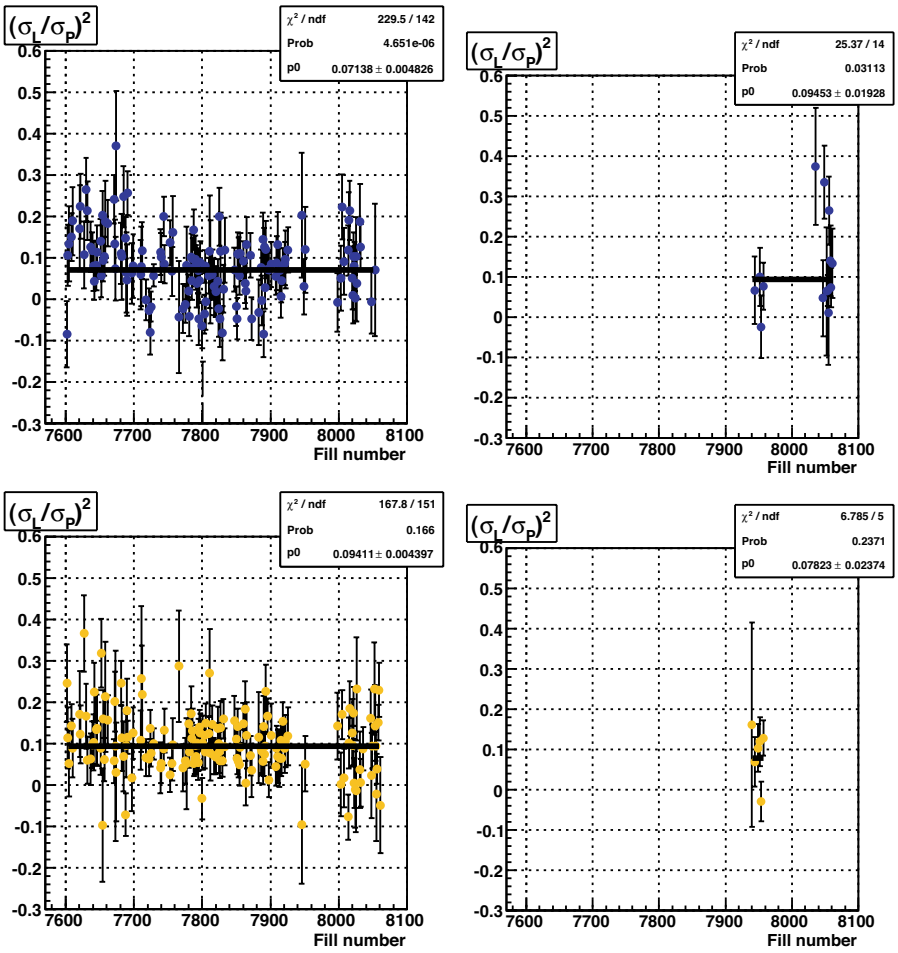


Fig. 23. The fill averaged horizontal $r_{\rm x}$ (left) and vertical $r_{\rm y}$ profiles for the blue (top) and yellow (bottom) beams. Data points are plotted for all physics stores at the beam energy of 100 GeV during Run06. Horizontal axis is the RHIC fill number. Solid lines show the averages.

where $C_{1\rm X}$ and $C_{1\rm Y}$ are the profile correction factors for the horizontal and vertical dimensions with the beam intensity profile weighted to the power of 1, respectively. $C_{1\rm X}$ can be described in a simple function of $r_{\rm x}$ as follows:

$$C_{1\rm X} = \frac{\int_{-\infty}^{\infty} dx \cdot \mathcal{P}(x) \cdot \mathcal{I}(x)}{\int_{-\infty}^{\infty} dx \cdot \mathcal{I}(x)} \tag{15}$$

$$= \frac{\int_{-\infty}^{\infty} dx \cdot e^{-\frac{x^2}{2\sigma_{\rm I}^2}} \cdot e^{-\frac{x^2}{2\sigma_{\rm P}^2}}}{\int_{-\infty}^{\infty} dx \cdot e^{-\frac{x^2}{2\sigma_{\rm I}^2}}} \tag{16}$$

$$= \frac{1}{\sqrt{1+(\frac{\sigma_{\rm I}}{\sigma_{\rm P}})^2}} \tag{17}$$

where the ratio $(\sigma_{\rm I}/\sigma_{\rm P})^2$ is substituted by $r_{\rm x}$ in Eq.12;

$$C_{1\rm X} = \frac{1}{\sqrt{1+r_{\rm x}}}. \tag{18}$$

Similarly for vertical direction,

$$C_{1\rm Y} = \frac{1}{\sqrt{1+r_{\rm y}}}. \tag{19}$$

On the other hand, as discussed in Section 7.1, the polarization profile needs to be weighted by both blue and yellow beam intensity profiles for the polarizations concerned by experiments $P_{\rm exp}$:

$$P_{\rm exp} = P_{\rm peak} \cdot C_{2\rm X} \cdot C_{2\rm Y}, \tag{20}$$

substitute $P_{\rm peak}$ using Eq.14,

$$P_{\rm exp} = \widetilde{P_{\rm pC}} \cdot \frac{C_{2\rm X}}{C_{1\rm X}} \cdot \frac{C_{2\rm Y}}{C_{1\rm Y}} \tag{21}$$

where $C_{2\rm X}$ and $C_{2\rm Y}$ are the profile correction factors for the horizontal and vertical dimensions with the beam intensity profile weight to the power of 2, respectively. Assuming the intensity profiles for the blue $\mathcal{I}_{\rm b}(x,y)$ and the yellow $\mathcal{I}_{\rm y}(x,y)$ beams are identical:

$$\mathcal{I}_{\rm b}(x) \approx \mathcal{I}_{\rm y}(x) \equiv \mathcal{I}(x) \tag{22}$$

$$\mathcal{I}_{\rm b}(y) \approx \mathcal{I}_{\rm y}(y) \equiv \mathcal{I}(y). \tag{23}$$

Under the assumptions above, the profile correction factors are given using Eq. 17;

$$C_{2\rm X} = \frac{\int_{-\infty}^{\infty} dx \cdot \mathcal{P}(x) \cdot \mathcal{I}_{\rm b}(x)\mathcal{I}_{\rm y}(x)}{\int_{-\infty}^{\infty} dx \cdot \mathcal{I}_{\rm b}(x)\mathcal{I}_{\rm y}(x)} \approx \frac{\int_{-\infty}^{\infty} dx \cdot \mathcal{P}(x) \cdot \mathcal{I}^2(x)}{\int_{-\infty}^{\infty} dx \cdot \mathcal{I}^2(x)} = \frac{1}{\sqrt{1+\frac{1}{2}r_{\rm x}}} \tag{24}$$

$$C_{2\rm Y} = \frac{\int_{-\infty}^{\infty} dy \cdot \mathcal{P}(y) \cdot \mathcal{I}_{\rm b}(y)\mathcal{I}_{\rm y}(y)}{\int_{-\infty}^{\infty} dy \cdot \mathcal{I}_{\rm b}(y)\mathcal{I}_{\rm y}(y)} \approx \frac{\int_{-\infty}^{\infty} dy \cdot \mathcal{P}(y) \cdot \mathcal{I}^2(y)}{\int_{-\infty}^{\infty} dy \cdot \mathcal{I}^2(y)} = \frac{1}{\sqrt{1+\frac{1}{2}r_{\rm y}}}. \tag{25}$$

The ratio $C_{2\rm X}/C_{1\rm X}$ in Eq. 21 is re-written using Eq. 18 $\sim$ Eq. 24;

$$\frac{C_{2\rm X}}{C_{1\rm X}} = \frac{\sqrt{1+r_{\rm x}}}{\sqrt{1+\frac{1}{2}r_{\rm x}}} \tag{26}$$

$$\approx \frac{(1+\frac{r_{\rm x}}{2})}{\sqrt{1+\frac{1}{2}r_{\rm x}}} \tag{27}$$

$$= \sqrt{1+\frac{1}{2}r_{\rm x}} \tag{28}$$

where the approximation

$$(1+r_{\rm x})^{\frac{1}{2}} \approx (1+\frac{r_{\rm x}}{2}) \tag{29}$$

was used for $r_{\rm x} \ll 1$. Similarly, the ratio $C_{\rm 2Y}/C_{\rm 1Y}$ in Eq. 21 are also calculated using Eq. 19 and Eq. 25;

$$\frac{C_{\rm 2Y}}{C_{\rm 1Y}} \approx \sqrt{1+\frac{1}{2}r_{\rm y}}. \tag{30}$$

The Eq. 21 is now calculable as a simple function of $r_{\rm x}$ and $r_{\rm y}$ using Eq. 28 and Eq. 30;

$$P_{\rm exp} = \widetilde{P_{\rm pC}} \cdot \sqrt{1+\frac{1}{2}r_{\rm x}} \cdot \sqrt{1+\frac{1}{2}r_{\rm y}}. \tag{31}$$

Thus polarization for the experiments are given by the measured polarization by pC polarimeters in scan mode with the polarization profile correction factors in both horizontal and vertical directions.

### 7.3. *Uncertainties*

Global errors, which are correlated from fill to fill are estimated and summarized in Table. 2. The total of global uncertainties are given by the quadratic some of each global errors. Besides global correlated errors, uncorrelated errors which applies to the average polarizations fill by fill, are estimated 2.4% as the energy correction, and 2.0% as the vertical profile uncertainties. The latter is originated from shortage of vertical profile measurements throughout Run06 and calculated from the possible range in $r_{\rm y}$ from a maximal variation ($\pm$RMS) from mean values $r_{\rm x}$ $((0.071 + 0.094)/2)$, as presented in Table.1, of the blue and yellow beams: $0.085\pm0.085$. This range was considered as a possible range in the average over vertical profile of a fill as well as possible fill from fill fluctuation in vertical profile. Resulting global systematic errors are estimated to be 4.7% and 4.8% for blue and yellow beams, respectively.

Table 2
The global systematic uncertainties.

| Errors | Blue ($\Delta P_{\rm B}/P_{\rm B}$) | Yellow ($\Delta P_{\rm Y}/P_{\rm Y}$) |
|---|---|---|
| Normalization Statistical | 2.3% | 2.4% |
| Normalization Horizontal Profile | 1.1% | 1.1% |
| Normalization H-Jet Molecular Contamination(6; 8) | 2.0% | 2.0% |
| Normalization H-Jet Other systematic(6; 8) | 1.3% | 1.5% |
| Polarization Profile for Experiments | 2.0% | 2.0% |
| Energy Correction | 2.4% | 2.4% |
| Total | 4.7% | 4.8% |

For the doubly polarized asymmetry measurements in experiments, the global uncertainty is given by the product of two beams:

$$\frac{\Delta P_{\rm B}\Delta P_{\rm Y}}{P_{\rm B}P_{\rm Y}} = 8.3\%. \tag{32}$$

## 8. Summary

The proton-carbon polarimeters were developed to measure the polarization of the polarized proton beams at RHIC. The left-right asymmetry of recoil carbon events through the elastic proton-carbon scattering provides polarization of the proton beam in a relative scale. The absolute scale is given by normalizing the average polarization of given period measured by the pC polarimeter against that of H-Jet polarimeter operated for the same period. Using an ultra-thin carbon ribbon target, the polarization measurement with a few percent statistical accuracy can be done within 20 to 30 seconds, providing fast feedback to the beam operation and experiments. pC polarimeters also provide detailed structures of the polarized beam by evaluating the polarization in bunch by bunch basis, mapping out the polarization profile across the beam. Such a capability plays important role for the accelerator tuning at RHIC. As a result of careful offline analysis, the global systematic errors of 4.7% and 4.8% for the average polarization in the blue and the yellow beams, respectively were achieved in Run06. The dominant uncertainty of which associated with the vertical polarization profile primarily due to shortage of measurements.

We thank the Collider Accelerator Department and the RHIC/AGS Operation Groups. We thank the Instrumentation Division at BNL for their work on the silicon detectors. This work is performed under the auspices of US DOE contract Nos. DE-AC02-98CH10886 and W-31-109-ENG-38, DOE grant No. DE-FG02-88ER40438, NSF grant PHY-0100348, and with support from RIKEN, Japan.

## Appendix A. Energy Loss Model

The $dE/dx$ of carbon ions in silicon calculated by MSTAR(15) "d-mode" was parameterized by a 5th order polynomial function:

$$\frac{dE}{dx} = c_1 + c_2 E + c_3 E^2 + c_4 E^3 + c_5 E^4 \tag{A.1}$$

The best fit result is shown in Fig. A.1 and the parameters are summarized in Table A.1. The best fit curve undershoots the MSTAR results below 1000 keV and overshoots above 1000 keV. The agreement in the region above 1000 keV is poor though, the concerned region for the present analysis is limited below 900 keV.

Table A.1
The best fit parameters of the 5th order polynomial fit on the $dE/dx$ calculation results by MSTAR d-mode.

| parameter | best fit value | error |
|---|---|---|
| $c_1$ | 0.37992 | $0.88500 \times 10^{-2}$ |
| $c_2$ | $0.86999 \times 10^{-2}$ | $0.33682 \times 10^{-4}$ |
| $c_3$ | $-0.76529 \times 10^{-5}$ | $0.33954 \times 10^{-7}$ |
| $c_4$ | $0.33133 \times 10^{-8}$ | $0.20693 \times 10^{-10}$ |
| $c_5$ | $-0.55159 \times 10^{-12}$ | $0.74799 \times 10^{-14}$ |

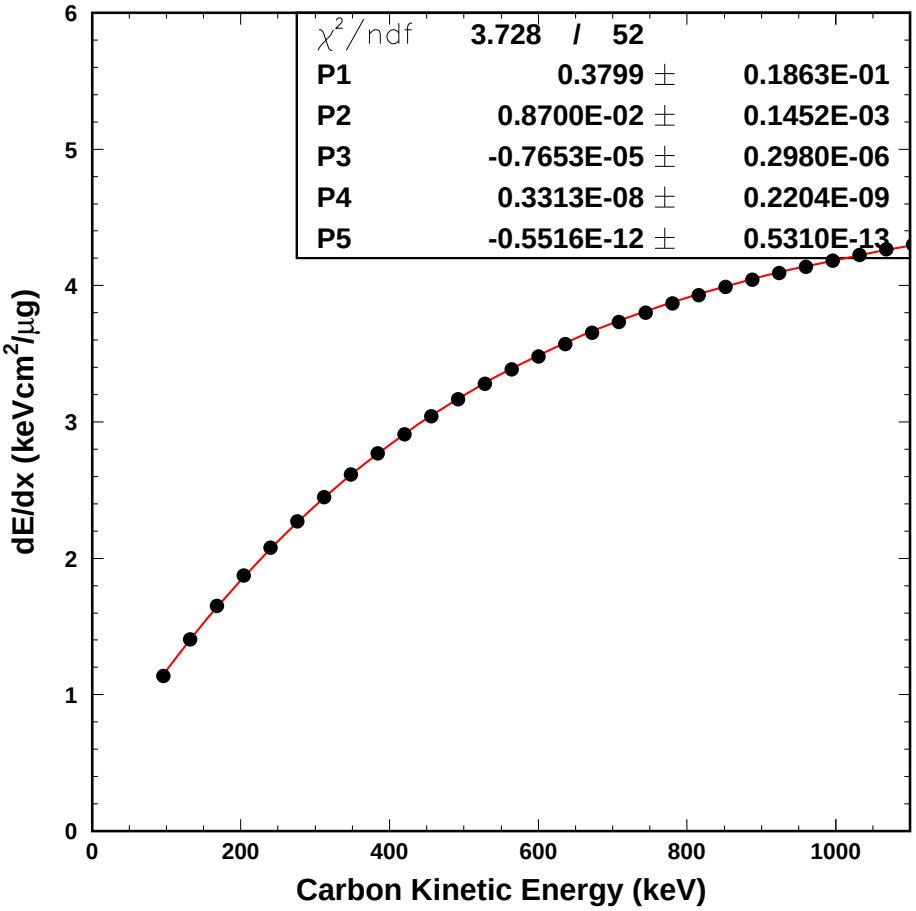


Fig. A.1. Calculated $dE/dx$ of carbon ion in silicon using the MSTAR "d-mode" (solid-circles) and the polynomial fit (solid curve).

Using the obtained $dE/dx$ function parameterized with the polynomials, the integrated energy losses over in the various given thicknesses of silicon are plotted in Fig. A.2 as a function of the kinetic energy of the carbon ion.

Assuming the incident energy of carbon $E$ is small enough to be stopped within the silicon, the observed energy $E_{\rm meas}$ by the sensitive region is the residual energy after the energy loss $E_{\rm loss}$ in the effective dead-layer at the surface silicon detectors.

$$E_{\rm meas} = E - E_{\rm loss} \tag{A.2}$$

Shown in Fig. A.3 is the measured energies as a function of the incident energy of the kinetic energy of carbon ion for the case of energy losses in various effective dead-layer thickness. Solid data points are calculated results using the best fit parameters of Eq.A.1. These data points are then fitted with a 5th order polynomial function.

$$E(x_{\rm dl}) = p_0(x_{\rm dl}) + p_1(x_{\rm dl})E_{\rm meas} + p_2(x_{\rm dl})E^2_{\rm meas} + p_3(x_{\rm dl})E^3_{\rm meas} + p_4(x_{\rm dl})E^4_{\rm meas} \tag{A.3}$$

where parameters $p_1 \sim p_5$ have a dependence on the effective dead-layer thickness $x_{\rm dl}$.

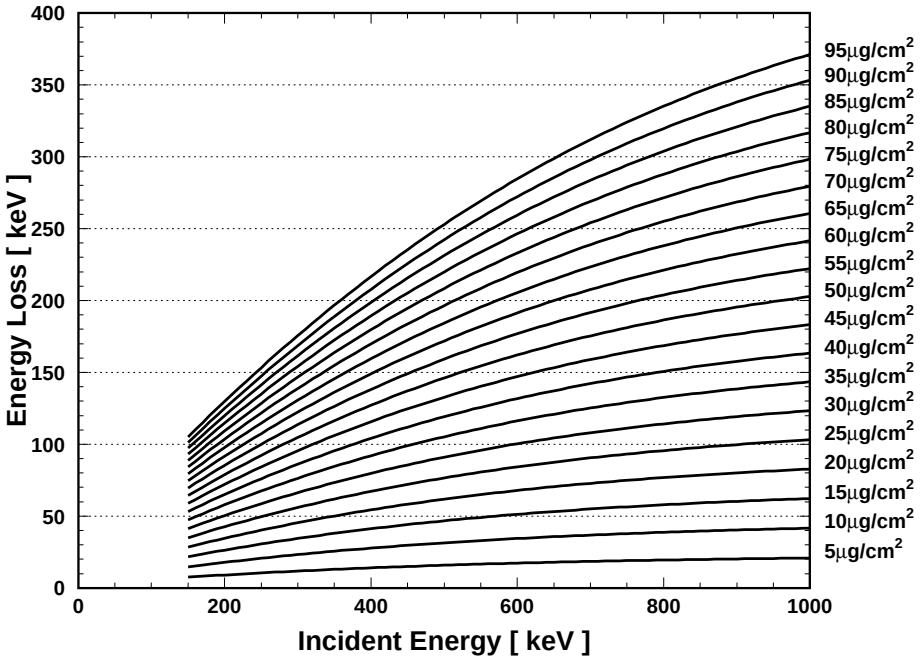


Fig. A.2. Integrated energy losses of a carbon ion in the various given thicknesses of silicon plotted as a function of the incident kinetic energy of the carbon ion.

The best fit results are superposed on the data points by red curves in the Fig. A.3. Mostly the fitting curves are flexible enough to reproduce all data points. As a final step to parameterize the function between $E$ and $E_{\rm meas}$ which can universally be used for various effective dead-layer thickness $x_{\rm dl}$, $x_{\rm dl}$ dependent coefficiencies $p_0 \sim p_4$ are then fitted with 4th order polynomial function as a function of $x_{\rm dl}$:

$$p_i(x_{\rm dl}) = P_1(i) + P_2(i)x_{\rm dl} + P_3(i)x_{\rm dl}^2 + P_4(i)x_{\rm dl}^3 \tag{A.4}$$

where $i$ runs for $0 \sim 4$. Shown in Fig.A.4 are fitting of coefficiencies $p_0 \sim p_4$ using Eq.A.4. Resulting best fit parameters of $P_1(i) \sim P_4(i)$ where $i : 0 \sim 4$ are summarized in Table A.2.

Table A.2
The best fit parameters of $P_1(i) \sim P_4(i)$ where $i : 0 \sim 4$.

| | $P_1(i)$ | $P_2(i)$ | $P_3(i)$ | $P_4(i)$ |
|---|---|---|---|---|
| $p_0(x_{\rm dl})$ | -0.5174 | 0.4172 | $0.3610 \times 10^{-2}$ | $-0.1286 \times 10^{-5}$ |
| $p_1(x_{\rm dl})$ | 1.0000 | $0.8703 \times 10^{-2}$ | $0.1252 \times 10^{-4}$ | $0.6948 \times 10^{-7}$ |
| $p_2(x_{\rm dl})$ | $0.2990 \times 10^{-5}$ | $-0.7937 \times 10^{-5}$ | $-0.2219 \times 10^{-7}$ | $-0.2877 \times 10^{-9}$ |
| $p_3(x_{\rm dl})$ | $-0.8258 \times 10^{-8}$ | $0.4031 \times 10^{-8}$ | $0.9673 \times 10^{-12}$ | $0.3661 \times 10^{-12}$ |
| $p_4(x_{\rm dl})$ | $0.3652 \times 10^{-11}$ | $-0.8652 \times 10^{-12}$ | $0.4059 \times 10^{-14}$ | $-0.1294 \times 10^{-15}$ |

In summary, the incident energy $E$ of carbon ion is calculated from the measured energy deposit $E_{\rm meas}$ in silicon with a given effective dead-layer thickness $x_{\rm dl}$:

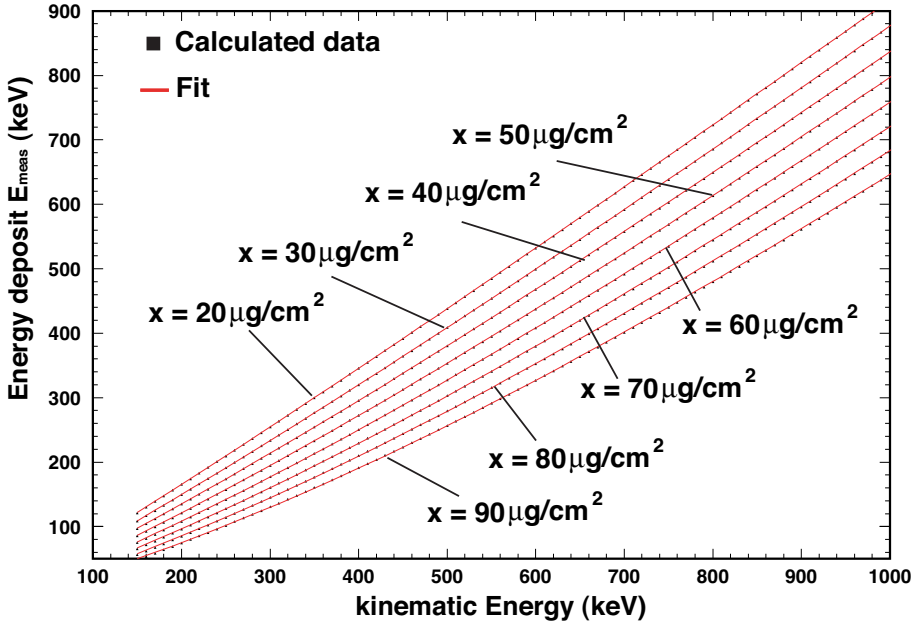


Fig. A.3. The measured energies as a function of the incident energy of the kinetic energy of carbon ion for the case of energy losses in various effective dead-layer thickness. Solid data points are calculated results using the best fit parameters of Eq.A.1. Red curves are fitting results using the 5th order polynomial function.

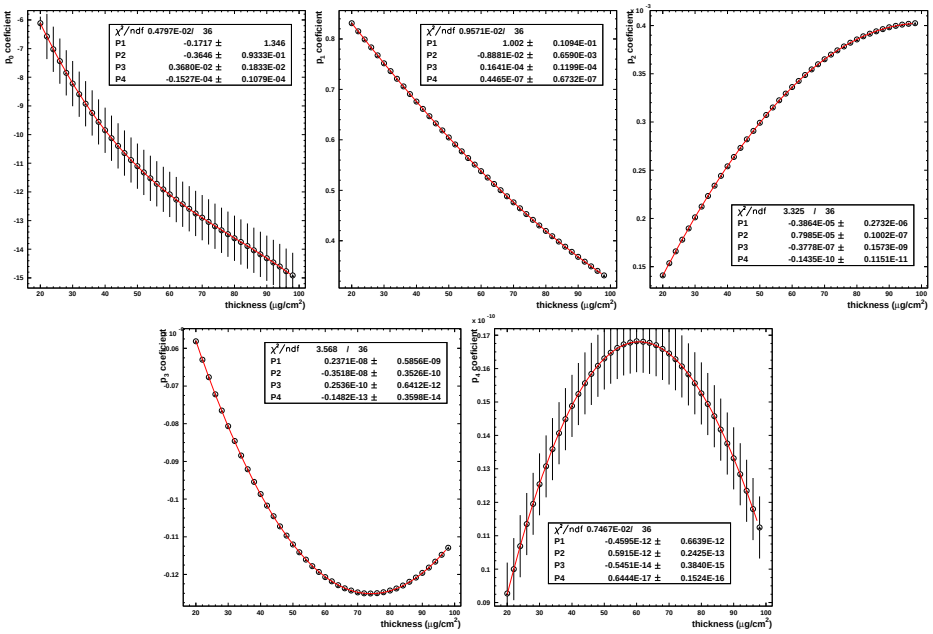


Fig. A.4. Polynomial fits to $x_{\mathrm{dl}}$ dependent coefficiencies.

$$
\begin{aligned}
E(x_{\rm dl}) &= p_0(x_{\rm dl}) + p_1(x_{\rm dl})E_{\rm meas} + p_2(x_{\rm dl})E^2_{\rm meas} + p_3(x_{\rm dl})E^3_{\rm meas} + p_4(x_{\rm dl})E^4_{\rm meas} \\
p_0(x_{\rm dl}) &= -0.5174 + 0.4172x_{\rm dl} + 0.3610\times10^{-2}x^2_{\rm dl} - 0.1286\times10^{-5}x^3_{\rm dl} \\
p_1(x_{\rm dl}) &= 1.0000 + 0.8703\times10^{-2} + 0.1252\times10^{-4} + 0.6948\times10^{-7} \\
p_2(x_{\rm dl}) &= 0.2990\times10^{-5} - 0.7937\times10^{-5}x_{\rm dl} - 0.2219\times10^{-7}x^2_{\rm dl} - 0.2877\times10^{-9}x^3_{\rm dl} \\
p_3(x_{\rm dl}) &= -0.8258\times10^{-8} + 0.4031\times10^{-8}x_{\rm dl} + 0.9673\times10^{-12}x^2_{\rm dl} + 0.3661\times10^{-12}x^3_{\rm dl} \\
p_4(x_{\rm dl}) &= 0.3652\times10^{-11} - 0.8652\times10^{-12}x_{\rm dl} + 0.4059\times10^{-14}x^2_{\rm dl} - 0.1294\times10^{-15}x^3_{\rm dl} \ .
\end{aligned}
$$

## References


[1] I. Alekseev et al., Nucl. Instr. Meth. A499, 392 (2003).
[2] M. Bai et al., Phys. Rev. Lett. 96, 174801 (2006).
[3] M. Harrison, T. Ludlam, S. Ozaki, Nucl. Instr. Meth. A499, 253 (2003).
[4] Ya.S. Derbenev et al., Part. Accel. 8, 115 (1978).
[5] A.N. Zelenski et al., Nucl. Instr. Meth. A536, 248 (2005).
[6] H. Okada et al. Phys. Lett. B638, 450 (2006)
[7] H. Okada, Ph. D thesis, Kyoto University (2006), unpublished.
[8] K.O. Eyser et al., RHIC/CAD Accelerator Physics Note Vol.274 (2007).
[9] O. Jinnouchi et al., RHIC/CAD Accelerator Physics Note Vol.171 (2004).
[10] I. Nakagawa et al., RHIC/CAD Accelerator Physics Note Vol.275 (2007).
[11] J. Tojo et al., Phys. Rev. Lett. 89, 052302 (2002).
[12] L. Trueman, hep-ph/0305085 (2003).
[13] A.N. Zelenski et al., Proceedings of PAC 1999, 1999, p.106.
[14] W.R. Lozowski and J.D. Hudson, Nucl. Inst. Meth. A303, 34 (1991), ibid Nucl. Instr. Meth. A334, 173 (1993).
[15] H. Paul and A. Schinner, Nucl. Instr. Meth. B179, 299 (2001). Ibid B195, 166 (2002). MSTAR ver.2.00 http://www.exphys.uni-linz.ac.at/Stopping/MstarWWW/MSTARInstr.htm
[16] S. Dhawan, private communication
[17] `http://direct.xilinx.com/bvdocs/publications/ds022.pdf`
[18] M. Bai et al., Nucl. Instr. Meth. A499, 372 (2003).